UCSF
UC San Francisco Electronic Theses and Dissertations

Title
Regulation of mitochondrial autophagy by huntingtin

Permalink
https://escholarship.org/uc/item/8kn713ss

Author
Margulis, Julia

Publication Date
2016

Peer reviewed|Thesis/dissertation

eScholarship.org Powered by the California Digital Library
University of California

Regulation of mitochondrial autophagy by huntingtin

by

Julia Margulis

DISSERTATION

Submitted in partial satisfaction of the requirements for the degree of

DOCTOR OF PHILOSOPHY

in

Neuroscience

in the

GRADUATE DIVISION

of the

UNIVERSITY OF CALIFORNIA, SAN FRANCISCO

DEDICATION AND ACKNOWLEDGEMENTS

First, I would like to thank my mentor, Steve Finkbeiner. I have grown tremendously as a person and a scientist in your lab, and I thank you for the opportunity to pursue a research project of my own design and to guide the project in the directions I considered interesting and relevant. Although it was, at times, a difficult and frustrating process, I feel that I have come out of graduate school a truly independent thinker and a scientist with a diverse set of skills. I am proud of the work I have done in your lab and am grateful for your guidance, patience, and scientific vision that helped me get to this point.

In addition, I would like to thank the members of the Finkbeiner lab for their advice, support, and friendship. The members of the lab, past and former, are an incredibly brilliant, generous, enthusiastic, and warm group of people and none of this would have been possible without the amazing community they created in the lab. In particular, I would like to acknowledge Mike Ando and Gaia Skibinski for being so generous with their time and scientific expertise.

I would also like to acknowledge Ben Shaby, Siddarth Samsi, and Aymeric Fouquier D'Herouël, who developed the Bayesian statistical modeling, automated mitochondrial morphology analysis, and automated mitochondrial mass analysis, respectively. In addition, Jinny Wong performed the electron microscopy analysis.

Finally, I would like to thank my family. It is their sacrifices that allow me to be here today, and my accomplishments are theirs as much as mine. My fiancé, Rob Bell, has also been there every step of the way through this process, and I couldn't have done it without his encouragement.

Regulation of mitochondrial autophagy by huntingtin

Julia Margulis

ABSTRACT

Huntington's disease (HD) is an inherited and incurable neurodegenerative disorder caused by an abnormal polyglutamine (polyQ) expansion in the huntingtin (Htt) protein. Dysregulation of protein quality control is a key event in HD pathogenesis. Here, we determined if mutant Htt (mHtt) also affects mitochondrial quality control via dysregulation of mitophagy. To monitor mitophagy in live neurons, we developed a sensitive and quantitative image-based technique utilizing automated microscopy and photoswitchable fluorescent proteins. We showed that neurons with diffuse mHtt exhibit mitochondrial damage and accelerated mitophagy, but neurons with inclusion bodies (IBs) do not. To unravel cause-and-effect relationships between mHtt, mitophagy and neurodegeneration, we collected longitudinal single cell measures of each variable and integrated these data into a Bayesian statistical model. From this model, we learned that diffuse mHtt is associated with increased mitophagy and neurodegeneration. Moreover, the total load of mHtt is a more important determinant of mitochondrial clearance than the presence of an IB. Finally, increased mitochondrial clearance is associated with reduced survival of neurons expressing mHtt. Thus, we uncovered a surprising relationship between mHtt expression, mitophagy, and neurodegeneration that has implications for the use of mitophagy pathways as therapeutic targets in HD.

TABLE OF CONTENTS

CHAPTER 1: INTRODUCTION

1.1 HUNTINGTON'S DISEASE……..2

1.2 INCLUSION BODY FORMATION IN HUNTINGTON'S DISEASE……..3

1.3 AUTOPHAGY……..3

1.4 AUTOPHAGY IN HUNTINGTON'S DISEASE……..4

1.5 MITOCHONDRIAL AUTOPHAGY……6

1.6 MITOCHONDRIAL DYSFUNCTION IN HUNTINGTON'S DISEASE…….7

1.7 CHALLENGES IN STUDYING MITOPHAGY IN NEURODEGENERATIVE DISEASE……9

1.8 AIMS OF THIS STUDY……...10

CHAPTER 2: DEVELOPMENT OF AN ASSAY TO MEASURE MITOCHONDRIAL AUTOPHAGY IN PRIMARY NEURONS

2.1 SELECTION OF A PHOTOSWITCHABLE FLUORESCENT PROTEIN……...13

2.2 VALIDATION OF THE OPTICAL PULSE-LABELING APPROACH……16

2.3 PHARMACOLOGICAL AND GENETIC MODULATION OF MITOCHONDRIAL HALF-LIFE……..21

2.4 CHARACTERIZATION OF BASAL MITOCHONDRIAL HALF-LIFE IN HEALTHY NEURONS……...24

CHAPTER 3: NEURONAL MITOPHAGY IS MODULATED BY HUNTINGTIN EXPRESSION AND PREDICTS NEURODEGENERATION

3.1 ESTABLISHMENT OF AN HD MODEL IN WHICH TO STUDY MITOPHAGY….27

3.2 EVALUATION OF MITOCHONDRIAL FUNCTION IN THE HD MODEL……..28

3.3 EVALUATION OF AUTOPHAGY RATES IN THE HD MODEL……32

3.4 EFFECT OF MUTANT HTT EXPRESSION ON MITOCHONDRIAL HALF-LIFE IN AN UNSTRATIFIED POPULATION OF NEURONS……34

3.5 MITOCHONDRIAL CLEARANCE RATES IN NEURONS WITH AND WITHOUT INCLUSION BODIES…….36

3.6 AUTOPHAGY RATES IN NEURONS WITH AND WITHOUT INCLUSION BODIES……38

3.7 SEQUESTRATION OF AUTOPHAGY PROTEINS BY INCLUSION BODIES……..40

3.8 RELATIONSHIP BETWEEN MITOPHAGY RATES AND NEURONAL SURVIVAL……...41

CHAPTER 4: MATERIALS AND METHODS

4.1 PLASMIDS…….48

4.2 shRNA…….48

4.3 LENTIVIRUS PRODUCTION……48

4.4 PHARMACOLOGY……..49

4.5 PRIMARY NEURON CULTURE……...49

4.6 IMMUNOCYTOCHEMISTRY……...50

4.7 QUANTITATIVE PCR WITH REVERSE TRANSCRIPTION……..50

4.8 MITOCHONDRIAL FUNCTION ASSESSMENT……51

4.9 ELECTRON MICROSCOPY……..51

4.10 CONFOCAL MICROSCOPY……51

4.11 AUTOMATED FLUORESCENCE MICROSCOPY……..52

4.12 IMAGE ANALYSIS……53

4.13 SURVIVAL ANALYSIS……54

4.14 MITOCHONDRIAL MORPHOLOGY ANALYSIS……...54

4.15 MITOCHONDRIAL MASS ANALYSIS……..56

4.16 BAYESIAN REGRESSION ANALYSIS……..57

4.17 FRET ANALYSIS……58

CHAPTER 5: DISCUSSION

5.1 CAVEATS OF THE MITOPHAGY ASSAY……..61

5.2 IMPLICATIONS FOR SELECTIVE NEURODEGENERATION……..64

5.3 MODELING HUNTINGTON'S DISEASE……65

5.4 POTENTIAL MECHANISMS OF HUNTINGTIN-MEDIATED MODULATION OF AUTOPHAGY AND MITOPHAGY……67

5.5 CLINICAL IMPLICATIONS……..69

BIBLIOGRAPHY……..70

APPENDIX……82

LIST OF TABLES

Table 2.1 Cox proportional hazards analysis of the effect of mitoEOS2 expression and photoswitching on neuronal survival……15

Table 3.1 Bayesian regression analysis of effects of mHtt expression level, IB formation, and mitochondrial clearance on neuronal survival……44

LIST OF FIGURES

Figure 2.1 Comparison of photoconversion efficiencies of various constructs……..14

Figure 2.2 Effect of photoswitching and mitoEOS2 levels on neuronal survival……...15

Figure 2.3 Additional characterization of a novel assay for mitochondrial autophagy in live neurons……...17

Figure 2.4 Effect of mitochondrial fission and fusion on photoswitched mitoEOS2 intensity……..19

Figure 2.5 Comparison of standard cytochrome oxidase subunit VIII (mito) and subunit IX of ATP synthase (Sub9) targeting sequence in the mitophagy assay……20

Figure 2.6 Characterization of a novel assay for mitochondrial autophagy in live neurons...23

Figure 2.7 Effect of Parkin KO on mitophagy……24

Figure 3.1 Mutant Htt induces neurodegeneration and mitochondrial dysfunction……28

Figure 3.2 Mitochondrial function assessment in neurons expressing wild-type and mutant Htt……..29

Figure 3.3 Assessment of mitochondrial morphology in neurons expressing wild-type and mutant Htt……..32

Figure 3.4 Mutant Htt increases autophagy……34

Figure 3.5 Effects of mutant Htt on mitochondrial localization to lysosomes and mitophagy……..36

Figure 3.6 Mitochondrial clearance rates differ in neurons containing diffuse mHtt or IBs.....38

Figure 3.7 LC3 levels in neurons expressing wild-type or mutant Htt……...40

Figure 3.8 Levels of autophagy-related proteins in cells with and without IBs……..41

Figure 3.9 Mitochondrial clearance determines neurodegeneration……...46

Figure 5.1 A model for the effect of mHtt on mitochondrial clearance, IB formation, and neurodegeneration……..68

Figure A.1 Effect of Atg5/12 knockdown on neuronal mitophagy and survival…….83

Figure A.2 Effect of mHtt expression on mitochondria-lysosome co-localization……..84

Figure A.3 Validation of FRET-based ATP assay……...85

Figure A.4 Characterization of ATP signal in primary neurons……..86

Figure A.5 Effect of low glucose media on neuronal survival and mHtt toxicity……...87

Figure A.6 Effect of CCCP treatment on TMRM intensity in neurons……...88

CHAPTER 1.

INTRODUCTION

1.1 HUNTINGTON'S DISEASE

Huntington's disease (HD) is an autosomal dominant neurodegenerative disorder that is uniformly fatal, affecting five to seven in 100,000 people (*1*). HD most often presents in the fourth or fifth decade of life, though onset has been documented from ages 1 to 80 years (*2*, *3*). The classic symptoms of HD include progressive motor dysfunction, psychiatric disturbances, and gradual dementia. Chorea is one of the most frequent symptoms and is most characteristic of the disease; however, the severity of chorea often correlates poorly with disease severity and progression (*4*). Age of disease onset may relate to the rate of disease progression, with disease progressing more quickly in juvenile onset HD (*5*).

The clinical progression of HD is paralleled by selective degeneration of the striatum, in particular the loss of striatal medium spiny neurons (MSNs) that express enkephalin and γ-aminobutyric acid (GABA) (*6*). The medial paraventricular region and tail of the caudate along with the dorsal putamen are the first brain regions to show significant atrophy (*7*). As the disease progresses, degeneration and significant volume loss also occurs in the cortex and later the globus pallidus and thalamus (*7*, *8*).

HD is caused by an expanded CAG repeat stretch in the huntingtin (Htt) gene. The CAG repeats translate into a homomeric polyglutamine (polyQ) stretch in the first exon of the Htt protein. Generally, 35 polyQ repeats or less are considered normal, whereas a Q length of greater than 35 almost invariably leads to disease. The number of polyQ repeats is inversely correlated with the age of onset of disease (*9*). PolyQ length explains more than seventy percent of the variation in the age of disease onset (*10*-*13*) and can be used to accurately predict disease incidence (*14*).

1.2 INCLUSION BODY FORMATION IN HUNTINGTON'S DISEASE

PolyQ expansion leads to altered Htt protein structure and aggregation of mutant Htt (mHtt) into inclusion bodies (IBs) (*15*). In HD brains, IBs are contained within the nucleus and, more commonly, the neuropil of striatal and cerebral cortical neurons. Other subcortical structures, such as the globus pallidus and the thalamus, exhibit fewer IBs (*16-18*). The appearance of IBs correlates with the onset of behavioral deficits in HD mouse models and human patients (*19*).

The mechanism of IB formation in HD is unclear, but the length of the polyQ repeat region correlates with the number of IBs in diseased brains (*7*, *20*). While the role IBs play in mediating cellular toxicity has been controversial, evidence suggests that the formation of IBs can be dissociated from neurodegeneration (*21-23*) and is a coping response to mHtt rather than a direct source of toxicity (*24*). In addition to aggregated mHtt, IBs contain ubiquitin, molecular chaperones, and proteasome subunits, suggesting that cells have insufficient capacity to clear misfolded mHtt (*18*, *25-27*). Further evidence suggests that cells can degrade IBs even after they form: Yamamoto and colleagues generated an inducible HD mouse model in which they terminated mHtt production after IBs and behavioral deficits arose. Turning off mHtt production caused IBs to disappear and reversed the behavioral deficits (*28*). Although this study demonstrated that IB formation is reversible, the investigators did not determine if IBs were cleared all at once or dissolved gradually. Later work showed that IBs in mHtt-expressing neurons can disappear abruptly (*24*, *29*), indicating that IBs can be cleared all at once. These findings suggest that neurons can spontaneously and rapidly metabolize IBs.

1.3 AUTOPHAGY

IB formation represents a mismatch between the production and clearance of aggregation-prone protein in neurons (*30*). Multiple protein quality control pathways, including macroautophagy, have been implicated in the clearance of mHtt IBs.

Macroautophagy (hereafter autophagy) is a conserved cellular pathway that degrades misfolded proteins, protein aggregates, and organelles. Autophagic degradation consists of three stages: autophagosome formation, maturation, and fusion with lysosomes (*31*). An isolation membrane forms during autophagosome formation that engulfs portions of cytoplasm containing proteins and organelles. Autophagosomes then fuse with lysosomes, leading to degradation of the autophagic cargo by lysosomal proteases (*31*).

The autophagy pathway can be regulated via the serine/threonine kinase mTOR (mammalian target of rapamycin), which suppresses autophagy under nutrient-rich conditions. Inhibition of mTOR by starvation leads to increased autophagy (*32*). Autophagy can also be regulated independently of mTOR; beclin-1 and calcium levels have both been implicated in autophagy regulation (*33*, *34*).

1.5 AUTOPHAGY IN HUNTINGTON'S DISEASE

Autophagy has been implicated in the pathogenesis of neurodegenerative diseases including Alzheimer's disease, (AD) Parkinson's disease (PD), and amyotrophic lateral sclerosis (ALS) (*35*, *36*). Autophagosome accumulation caused by impaired clearance of autophagosomes has been observed in AD (*37*), while defects in mitochondrial autophagy and general autophagy

deregulation have been observed in PD (*38*, *39*). In ALS, both impaired autophagosome trafficking and increased autophagy have been observed (*40*, *41*). These neurodegenerative diseases have both genetic and sporadic forms, and multiple toxic proteins have been implicated in their pathogenic mechanisms; thus, it is unsurprising that multiple conflicting reports of autophagy phenotypes in these diseases exist. HD, on the other hand, is a genetic disease caused by one protein, huntingtin; however, the exact changes in the autophagy pathway that exist in HD are yet to be established. Various lines of evidence from a number of different model systems implicate autophagy dysregulation as a contributor to or mitigating factor in HD (*42*).

Initial evidence has pointed to increased autophagy in the context of HD. For example, increased numbers of autophagosomes and increased autophagic flux have been observed in HD brains and cells (*43-45*). A potential mechanism for this activation may be the sequestration and inactivation of mTOR by mHtt (*46*). Conversely, autophagosomes in mHtt-expressing cells were observed to be empty of cargo, implying a cargo loading defect and insufficient autophagy in HD (*45*). Thus, although mHtt-expressing neurons seem to exhibit increased autophagosome production, autophagic cargo in these cells is incompletely degraded. Mutant Htt has also been shown to affect autophagosome motility and the fusion process between autophagosomes and lysosomes (*47*). In addition, deletion of the polyQ stretch in wild-type Htt has been associated with increased autophagy induction (*48*).

Autophagy protein and gene expression levels have also been shown to be altered in HD. Expression of autophagy genes such as *LC3A*, *ULK2*, and *LAMP2* are altered in the caudate nucleus of HD patients (*49*). Changes in levels of genes encoding vacuolar proton channel

complex subunits, which are involved in autophagy (*43*, *46*), were also found in human HD brains (*50*). In addition, levels of Omi/HtrA2, a chaperone and protease known to regulate autophagy (*51*), are reduced in striatal neurons by mHtt expression (*52*). However, other studies found no difference in autophagy flux rates, autophagy gene levels, or autophagy protein levels in the context of HD (*53*).

Other evidence suggests that Htt itself can regulate autophagy, and that a loss of Htt function results in insufficient autophagy. In addition to its effects on autophagosome dynamics (*47*), Htt has been shown to contain an autophagy-inducing domain that is regulated by myristoylation (*54*). Other studies have posited that Htt may have evolved from yeast autophagy proteins, as certain domains of Htt exhibit high homology with yeast Atg23, Atg11, and Vac8 (*55*). These proteins are involved in selective vacuolar targeting, implicating Htt in the regulation of selective autophagy. Indeed, in mammalian cells, Htt may have a role as a scaffold for selective autophagy (*56*, *57*). Overall, the effect of mHtt on autophagy is controversial, and the downstream effects of Htt-mediated autophagy modulation on neuronal health are unclear.

1.4 MITOCHONDRIAL AUTOPHAGY

Although autophagy was initially identified as a bulk clearance mechanism activated during starvation, selective forms of autophagy exist as well. In particular, autophagy can specifically degrade damaged or dysfunctional mitochondria through a process called mitochondrial autophagy, or mitophagy. As mitochondria are essential in regulating cellular energy homeostasis and cell death, the removal of damaged mitochondria via mitophagy is critical to maintaining normal cellular function. In addition to the induction of general autophagy,

mitophagy requires an additional step involving priming of damaged mitochondria for recognition and degradation (*58*).

The molecules involved in carrying out mitophagy have primarily been studied in yeast. In addition to the cellular machinery involved in general autophagy, the mitochondrial outer membrane protein autophagy-related gene 32 (ATG32) acts as an "autophagy receptor" that recruits autophagic machinery to damaged mitochondria for their selective degradation (*59*). No mammalian homologue has been identified for ATG32; in fact, mammalian mitophagy differs significantly from yeast mitophagy both in terms of initiating drivers as well as molecular machinery involved (*58*).

The major initiating drivers of mitophagy in mammalian cells include mitochondrial permeability transition and depolarization, mitochondrial fragmentation, and cellular ATP depletion (*58*). A number of proteins have been identified as players in mammalian mitophagy, including ULK1, Ambra1, Smurf1, Nix/Bnip3, optineurin, NDP52, and PINK1/Parkin (*38*, *60-64*). PINK1 and Parkin are of particular interest, as mutations in these genes have been found to be associated with familial forms of Parkinson's disease (*65*). However, many of these pathways remain validated only in immortalized cell lines. It is likely that mitophagy in neuronal cells is induced and regulated differently than in non-neuronal cells due to the unique bioenergetic requirements inherent to neurons (*66-68*).

1.6 MITOCHONDRIAL DYSFUNCTION IN HUNTINGTON'S DISEASE

Neurons are particularly sensitive to mitochondrial dysfunction due to their increased reliance on oxidative phosphorylation compared to other cell types (*66*). Neurons also exhibit an extremely polarized morphology, necessitating the delivery of mitochondria to synapses far from the cell body in order to meet the high energetic requirements of synaptic transmission (*69*). In addition, as neurons are postmitotic, mitochondrial quality control mechanisms are critical, as cells cannot simply divide to eliminate damaged and dysfunctional mitochondria (*70*). Many proteins implicated in neurodegenerative disease have been shown to induce mitochondrial dysfunction, providing a potential explanation for the neurological phenotypes present in these diseases (*71*).

Mitochondrial dysfunction is a well-established feature of HD. Defects in mitochondrial trafficking, morphology, Ca^{2+} handling, and ATP production have been demonstrated in HD models as well as HD patient brains (*72*-*75*). Mitochondrial biogenesis is also reduced in the presence of mHtt, potentially due to mHtt-mediated transcriptional suppression of PGC-1α (*76*). Insufficient mitochondrial ATP production and depolarization can induce a compensatory mitophagy response meant to clear dysfunctional organelles (*77*). In addition, fragmented mitochondria, such as those observed in the presence of mHtt, tend to be more defective and are more readily degraded via mitophagy (*78*, *79*). Thus, mHtt-expressing neurons would be expected to upregulate mitophagy in response to the mitochondrial dysfunction caused by mHtt. However, the few studies that have directly addressed this question showed reduced mitophagy (*45*, *47*, *80*, *81*). Other studies have shown defects in selective autophagy, including mitophagy, due to a purported role for Htt as a scaffold for protein complexes involved in selective autophagy (*56*, *57*). Although mitophagy has been implicated as a driver of neurotoxicity in a

number of neurodegenerative disease, including HD (*82*), it is still unclear how alterations in mitophagy are related to neuronal longevity.

1.7 CHALLENGES IN STUDYING MITOPHAGY IN NEURODEGENERATIVE DISEASE

A major obstacle to the study of mitophagy in HD has been the absence of a robust assay to measure mitochondrial clearance in neurons. Existing assays that rely on co-localization of autophagic markers with mitochondria, or quantification of autophagosomes containing mitochondria via electron microscopy, are snapshots of a dynamic process and do not capture the rate of mitochondrial clearance (*83*). Rates of flux inferred from such snapshot measures have serious confounds – an increase in autophagosome number does not necessarily indicate increased autophagic flux, for example (*84*). In addition, these assays have been generally performed in non-neuronal cells, which likely regulate mitophagy differently than neurons do. Indeed, neurons have been shown to be much more dependent on oxidative phosphorylation and therefore on mitochondrial function than immortalized or dividing cells, which have a comparatively larger capacity to generate ATP from glycolysis (*66*). As neurons are the primary cell type affected in HD and other neurodegenerative diseases, it is critical that a study of mitophagy in HD be performed in the relevant cell type.

In addition to measuring mitophagy in the relevant cell type, performing the measurement in individual cells is also critical. Cells vary widely in their level of mHtt expression and localization, which can affect mitophagy rates and be missed in a population-based measure (*85*). In addition, increasing evidence points to cell-specific differences in mitochondrial function and

turnover that could explain the differential susceptibilities of cell populations in HD and other neurodegenerative diseases, such as Parkinson's disease (*86-88*). Thus, an assay that can detect individual differences in mitochondrial clearance is key to understanding the role of cell-to-cell variability in pathogenesis.

1.8 AIMS OF THIS STUDY

The relationship between mHtt expression, IB formation, mitochondrial quality control via mitophagy, and neurodegeneration has been difficult to address. In particular, the effect of mHtt expression on mitophagy, and whether this change is relevant to neuronal survival in HD models, has been challenging to determine using standard snapshot measures of mitophagy and neuronal survival. These conventional approaches have yielded contradictory results because they lack the sensitivity to measure mitochondrial turnover on a single cell basis and cannot gather enough longitudinal data to relate these turnover measures to cellular fate.

In Chapter 2, we developed a novel assay capable of measuring mitophagy in single neurons. The output of this assay is a mitochondrial half-life per neuron, allowing us to make observations regarding the variability of mitochondrial half-life across neuronal populations, and the responsiveness of this half-life to various pharmacological and genetic manipulations.

In Chapter 3, we used this technique to uncover previously unknown relationships between Htt expression, IB formation, mitochondrial clearance, and neuronal survival. Neurons with mHtt IBs had slower rates of mitochondrial clearance than neurons expressing diffuse mHtt. However, we found that the load of mHtt was a stronger determinant of mitochondrial clearance rates than

the formation of the IB itself. In addition, we found that mitochondrial clearance was a negative predictor of neuronal survival in the context of wild-type and mutant Htt, and a positive predictor of neuronal survival in neurons expressing GFP alone. These data implicate mitochondrial clearance pathways as a therapeutic target in HD and other neurodegenerative diseases.

CHAPTER 2.

DEVELOPMENT OF AN ASSAY TO MEASURE MITOCHONDRIAL AUTOPHAGY IN PRIMARY NEURONS

2.1 SELECTION OF A PHOTOSWITCHABLE FLUORESCENT PROTEIN

Given the critical importance of mitochondrial function to HD and the substantial limitations of existing assays of mitochondrial turnover, we set out to develop a new assay that could measure mitochondrial turnover dynamically over time in primary neurons at a single cell level. We utilized a technique known as optical pulse labeling (OPL), which uses photoconvertible proteins, such as EOS2 or Dendra2, that irreversibly switch their spectral properties when exposed to short-wavelength light. We have previously developed OPL-based assays to measure clearance of LC3, Htt, and TDP43 in individual neurons, which have allowed us to make novel observations regarding cell-to-cell differences in clearance capacity and link these measures to cell fate (*85*, *89*). Unlike canonical metabolic pulse chase-based measures of protein degradation, OPL assays are not confounded by cell death during the chase period or aggregation of the target protein (*89*).

We first considered the choice of photoswitchable protein to use for the development of this assay. The expression levels and photoswitching efficiencies of various tagged and untagged versions of Dendra2 and EOS2, the two most well-characterized green-to-red photoswitchable proteins (*90*, *91*), were measured (Figure 2.1). Although EOS2 expression was low overall, its photoconversion efficiency was the highest of all proteins tested (Fig 2.1b). Thus, EOS2 was selected as the photoswitchable protein to be used in this assay.

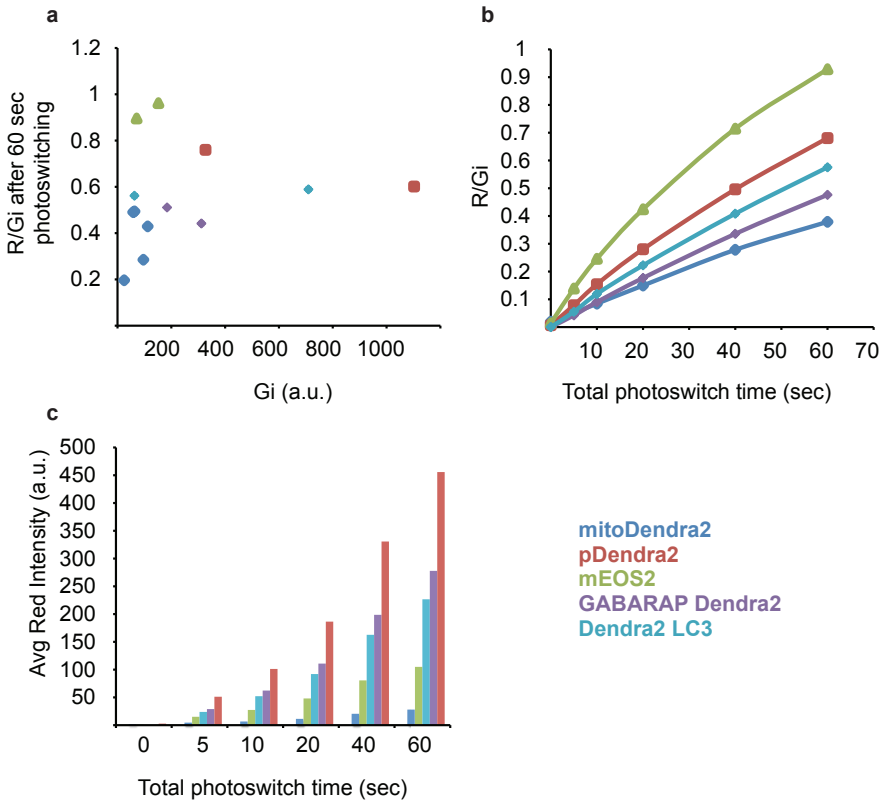


Figure 2.1 Comparison of photoconversion efficiencies of various constructs. (a) Red intensity (R) over green intensity (Gi) was measured after 60 seconds of photoswitching with 405 nm light. Each point represents data from an individual neuron. (b) R/Gi with increasing photoswitching time. (c) Average red intensity with increasing photoswitching time. n=2-5 neurons per condition for (b) and (c).

In order to measure mitophagy, we targeted EOS2 to mitochondria using a canonical 25 a.a. targeting sequence from cytochrome oxidase subunit VIII (*92*) (mitoEOS2) and expressed the construct in rat primary cortical neurons. Approximately 24 hours post-transfection, neurons were photoconverted with a 4-second pulse of 405-nm light and longitudinally imaged using robotic microscopy (RM), which is capable of returning to the same cell repeatedly over time (*93*). This photoswitching pulse is not toxic to neurons (Figure 2.2 and Table 2.1). In addition, the level of mitoEOS2 plasmid transfected was titrated such that the expression of mitoEOS2 alone was not toxic to the neurons (Figure 2.2 and Table 2.1).

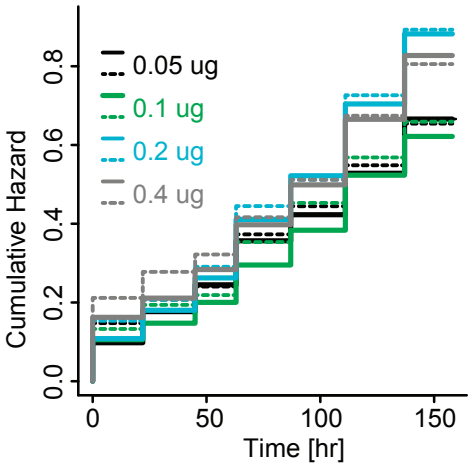


Figure 2.2 Effect of photoswitching and mitoEOS2 levels on neuronal survival. Cumulative hazard of neurons transfected with varying levels of mitoEOS2 and either photoswitched with a 4 second pulse of 405 nm light (dashed lines) or not photoswitched (solid lines). n=250-380 neurons per group.

Table 2.1 Cox proportional hazards analysis of the effect of mitoEOS2 expression and photoswitching on neuronal survival

Covariate	Hazard ratio	p-value
0.05	1.022	n.s.
0.05 PS	0.972	n.s.
0.1	0.965	n.s.
0.2	1.414	**
0.2 PS	1.358	**
0.4	1.447	**
0.4 PS	1.262	*
mitoEOS2 expression	0.999	***

Table 2.1 Cox proportional hazards analysis of the effect of mitoEOS2 expression and photoswitching on neuronal survival. A Cox proportional hazards analysis was performed to compare neuronal survival across groups of neurons expressing different levels of mitoEOS2. All hazard ratios are in comparison to 0.1 PS. According to this analysis, expression of mitoEOS2 at 0.05 µg or 0.1 µg per well does not affect neuronal toxicity. Photoswitching neurons expressing mitoEOS2 at either of these DNA levels also does not affect neuronal toxicity. However, expression of 0.2 µg or 0.4 µg of mitoEOS2 DNA per well does increase neuronal toxicity. The effect on hazard of mitoEOS2 expression across all conditions (mitoEOS2 expression covariate) is negative and significant, indicating that mitoEOS2 expression is actually associated with reduced neuronal toxicity. PS: photoswitched.

Single-cell red fluorescence intensities for each cell were normalized to the red fluorescence immediately after photoconversion and a mitochondrial half-life was calculated for each individual cell using the standard half-life equation.

2.2 VALIDATION OF THE OPTICAL-PULSE LABELING APPROACH

A highly desirable feature of any reporter system is that the biology being reported is not significantly affected by the reporter itself. To test whether mitoEOS2 affected the biology we sought to measure, we investigated whether the rate of mitochondrial turnover was affected by the levels of mitoEOS2 at a single cell level. (Fig 2.3b). Initial red intensity is a good proxy for total construct expression, as initial red intensity is highly correlated with initial green EOS2 intensity (Fig. 2.3a). We found no correlation between initial red intensity and half-life, indicating that the expression level of mitoEOS2 does not affect the half-life measurement (Fig. 2.3b).

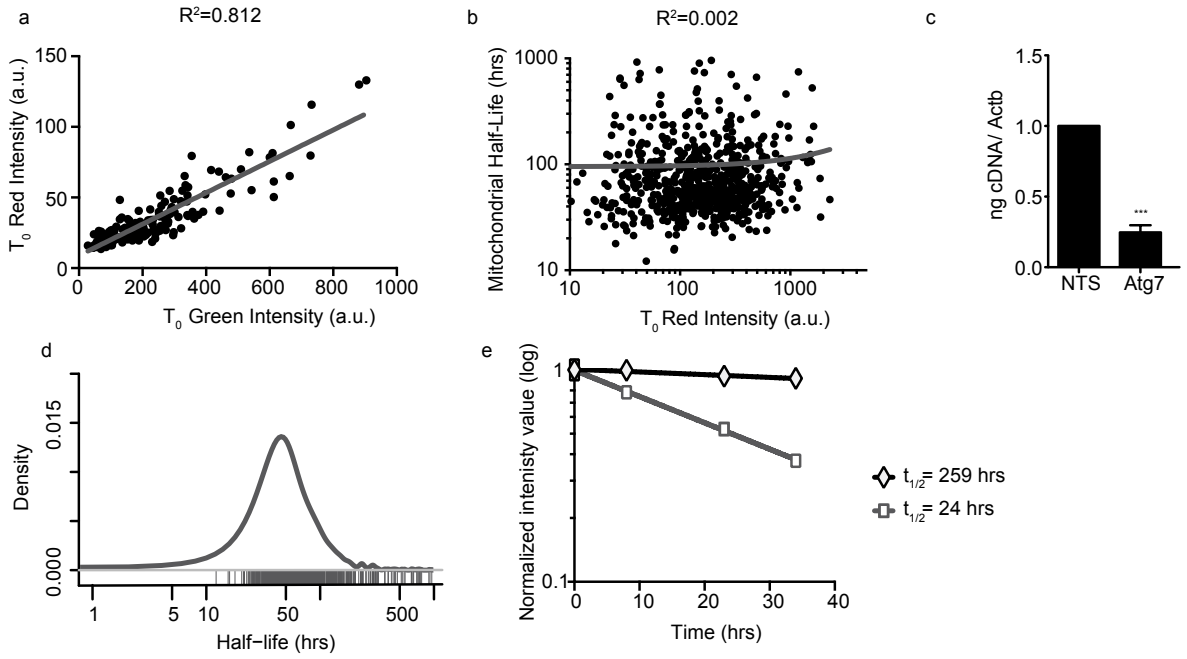


Figure 2.3 Additional characterization of a novel assay for mitochondrial autophagy in live neurons. (a) Correlation of initial (T_0) red mitoEOS2 intensity (the intensity of red mitoEOS2 at the first imaging timepoint) with T_0 green mitoEOS2 intensity and mitoEOS2 plasmid expression level. T_0 red mitoEOS2 intensity and T_0 green mitoEOS2 intensity are highly correlated. R^2=0.812, p<0.0001. (b) Relationship between mitochondrial half-life and T_0 red mitoEOS2 intensity. No relationship was observed. R^2=0.002, p=0.28. (c) Effect of Atg7 shRNA on Atg7 mRNA levels. Infection of primary neurons with Atg7 shRNA-expressing lentivirus results in a 75% reduction in Atg7 mRNA levels as measured by qRT-PCR. Complementary DNA (cDNA) levels were normalized to levels of actin cDNA (Actb) in each sample. (d) Distribution of mitochondrial half-lives across a population of wild-type neurons. The mean is approximately 100 hours and can vary by as much as 2 orders of magnitude. (e) Decay profiles of cells with short and long mitochondrial half-lives. Cells with both short and long half-lives display linear decay profiles, indicating that the variation in half-life at a single cell level reflects real differences in mitochondrial clearance rates. Means across conditions were compared using Student's t-test. ***, p<0.001

As mitochondria are dynamic organelles, and undergo constant fission and fusion, we sought to ensure that mitochondrial fission and fusion dynamics did not quench or artificially amplify the red fluorescence signal that we used as a measure of mitochondrial clearance. In order to determine the effect of mitochondrial fission and fusion on red mitoEOS2 fluorescence, we measured this fluorescence in mitochondria that were undergoing fission and fusion or staying stable. As individual neuronal mitochondria can be difficult to distinguish from one another due to the high density of mitochondria in the cell body, we used HeLa cells, which have a much more defined mitochondrial reticulum. HeLa cells were transfected with mito-GFP and imaged

continuously for ~2 min at 3 sec intervals. Portions of the image containing individual mitochondria that underwent fission, fusion, or stayed stable were background subtracted, and the intensity of the mitochondria in the image was measured over the imaging period (Fig. 2.4). We did not observe any large changes in fluorescence during mitochondrial fission or fusion (Fig. 2.4d,f). Thus, mitochondrial fission and fusion dynamics do not artificially affect mitoEOS2 fluorescence in ways that could affect the mitochondrial half-life measurement. However, we did not assay the effect of mitochondrial transport into and out of the cell body, and cannot definitely rule out the possibility that mitochondrial transport dynamics affect the half-life measurement.

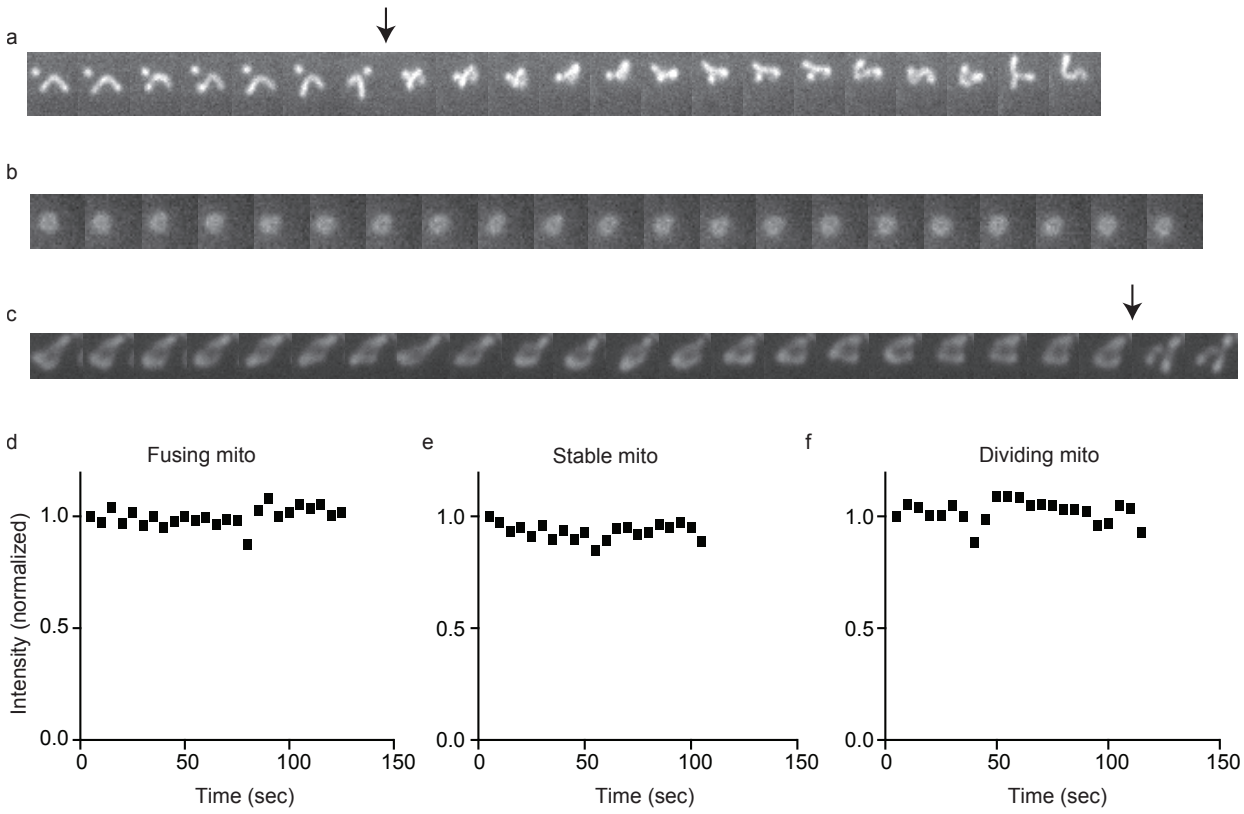


Figure 2.4 Effect of mitochondrial fission and fusion on photoswitched mitoEOS2 intensity. (a) Time series of two mitochondria labeled with mitoEOS2 fusing into one organelle. HeLa cells were transfected with mitoEOS2, photoswitched, and imaged at 5 sec intervals for ~2 min. Approximate time of fusion is marked by an arrow. (b) Time series of a mitochondrion labeled with mitoEOS2 that neither fuses nor divides. (c) Time series of a mitochondrion labeled with mitoEOS2 that divides into two mitochondria. Approximate time of division is marked by an arrow. (d) Integrated intensity of fusing mitochondria over time. (e) Integrated intensity of stable mitochondrion over time. (f) Integrated intensity of dividing mitochondrion over time.

Mitochondria have multiple compartments, including the matrix, the intermembrane space, and the outer membrane. Outer membrane proteins and proteins destined for the intermembrane space can be degraded both by autophagy (when the entire organelle is degraded) as well as the cytoplasmic ubiquitin proteasome system (UPS), while matrix proteins are primarily degraded via mitophagy (*94*). We targeted the EOS2 probe to the matrix such that its clearance would be most directly related to mitophagy. However, we wanted to ensure that our choice of specific matrix targeting sequence did not affect the mitochondrial clearance measurement. In order to

test this, we made an additional EOS2 construct using the matrix targeting sequence from *Neurospora* F_0 ATPase subunit 9 (Sub9EOS2) (*95*). We then assayed expression, toxicity, and mitochondrial clearance measured with the two matrix targeting sequences (Fig. 2.5). MitoEOS2 was expressed at 0.1 µg per well, while Sub9EOS2 was expressed at 3 different levels: 0.1 µg, 0.2 µg, and 0.4 µg. Initial red intensity after photoswitching (T_0 red intensity) was slightly elevated in all the Sub9EOS2 conditions; however, only Sub9EOS2 expressed at 0.4 µg was statistically significantly higher than mitoEOS2 (Fig. 2.5a). The mitochondrial half-life measured using mitoEOS2 and Sub9EOS2 was the same across all conditions (Fig 2.5b). Finally, survival across all populations of neurons expressing Sub9EOS2 was significantly improved compared to neurons expressing mitoEOS2 (Fig 2.5c). Thus, using a different matrix targeting sequence did not significantly affect the half-life measurement using the mitophagy assay we developed.

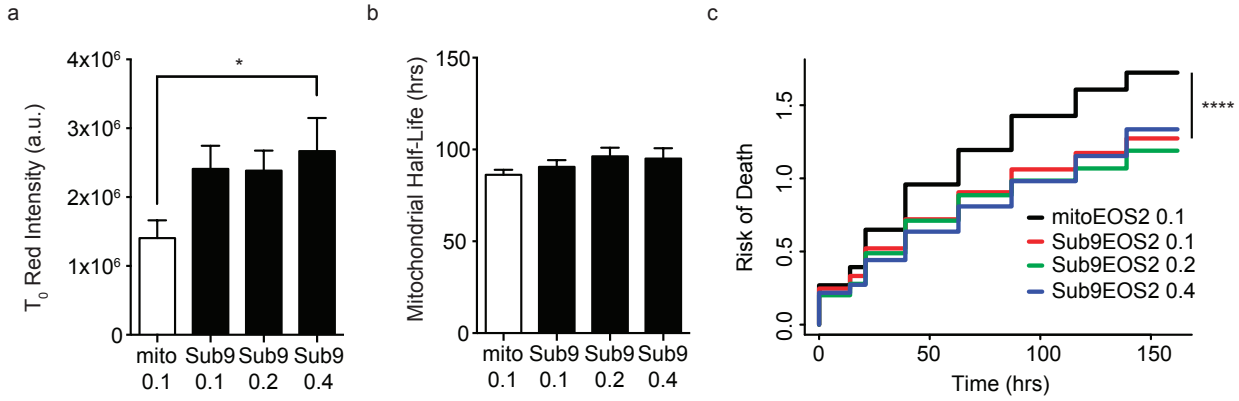


Figure 2.5 Comparison of standard cytochrome oxidase subunit VIII (mito) and subunit IX of ATP synthase (Sub9) targeting sequences in the mitophagy assay. (a) Photoswitched mitoEOS2 intensity at first timepoint post-transfection (T_0) in cells transfected with 0.1 µg mitoEOS2 (mito 0.1), 0.1 µg Sub9EOS2 (Sub9 0.1), 0.2 µg Sub9EOS2 (Sub9 0.2), and 0.4 µg Sub9EOS2 (Sub9 0.4). Sub9 0.4 intensity was significantly higher than mitoEOS2 intensity. (b) Mitochondrial half-life measured in cells transfected with mitoEOS2 and various levels of Sub9EOS2. No difference in mitochondrial half-life was measured in cells in which mitochondria were labeled with the Sub9 targeting sequence. (c) Survival curves from cells transfected with mitoEOS2 and various levels of Sub9EOS2. Sub9 0.1 had significantly improved survival compared to mitoEOS2 0.1. Means across conditions were compared using 1-way ANOVA with Tukey's correction. Survival curves were compared using a log-rank test. *, $p<0.05$; ****, $p<0.0001$

2.3 PHARMACOLOGICAL AND GENETIC MODULATION OF MITOCHONDRIAL HALF-LIFE

We next wanted to determine whether the change in red fluorescence provides a reliable measure of mitochondrial clearance. We used several tools that promote or retard mitochondrial clearance. To induce mitochondrial clearance, rat primary cortical neurons co-expressing mitoEOS2 and EGFP were treated with 1 μM carbonyl cyanide-*4*-(trifluoromethoxy)phenylhydrazone (FCCP) for 4 hours and mitochondrial half-life was measured as described above. FCCP causes mitochondrial depolarization, which leads to increased mitochondrial elimination via mitophagy (*61*). Using the mitoEOS2 OPL assay, we measured a significantly reduced mean mitochondrial half-life after FCCP treatment (Fig 2.6b, left). As these experiments are conducted in primary cultures, large effects in subpopulations might be responsible for the FCCP effect on mitochondrial clearance that we observed. Fortunately, the OPL method generates half-life measurements from individual cells. Thus, we can plot the distribution of single cell half-lives and compare the effects of FCCP treatment on that distribution. Indeed, FCCP treatment shifted the distribution to the left, towards shorter half-lives (Fig. 2.6b, right). These data indicate that the mitoEOS2 OPL assay reliably detects increased mitochondrial clearance.

We next sought to test whether the clearance was mitophagy-dependent by treating cells with autophagy and mitophagy inhibitors. MitoEOS2-expressing neurons were treated with 5 or 10 mM 3-methyladenine (3-MA) for 42−48 hours. 3-MA inhibits autophagy by inhibiting autophagosome synthesis, and autophagosomes engulf mitochondria during mitophagy. Both 5 and 10 mM 3-MA increased mean mitochondrial half-life in a dose-dependent manner (Fig. 2.6c,

left) and shifted the distribution of half-lives to the right (Fig. 2.6c, right), supporting the idea that the assay measures mitochondrial clearance via mitophagy specifically.

As pharmacological manipulations often have off-target effects, we sought to validate the mitoEOS2 assay by genetic modulation. Atg7 (autophagy-related protein 7) is required to lipidate LC3 and for the progression of autophagy (*96*). To test whether knockdown of Atg7 affected mitochondrial half-life measured with the OPL assay, neurons were co-transfected with shRNA against Atg7 or non-targeting shRNA and mitoEOS2. Atg7 shRNA knocked down endogenous Atg7 levels by ~75% (Fig. 2.3c). Atg7 knockdown increased mean mitochondrial half-life (Fig. 2.6d, left) and shifted the half-life distribution to the right (Fig. 2.6d, right).

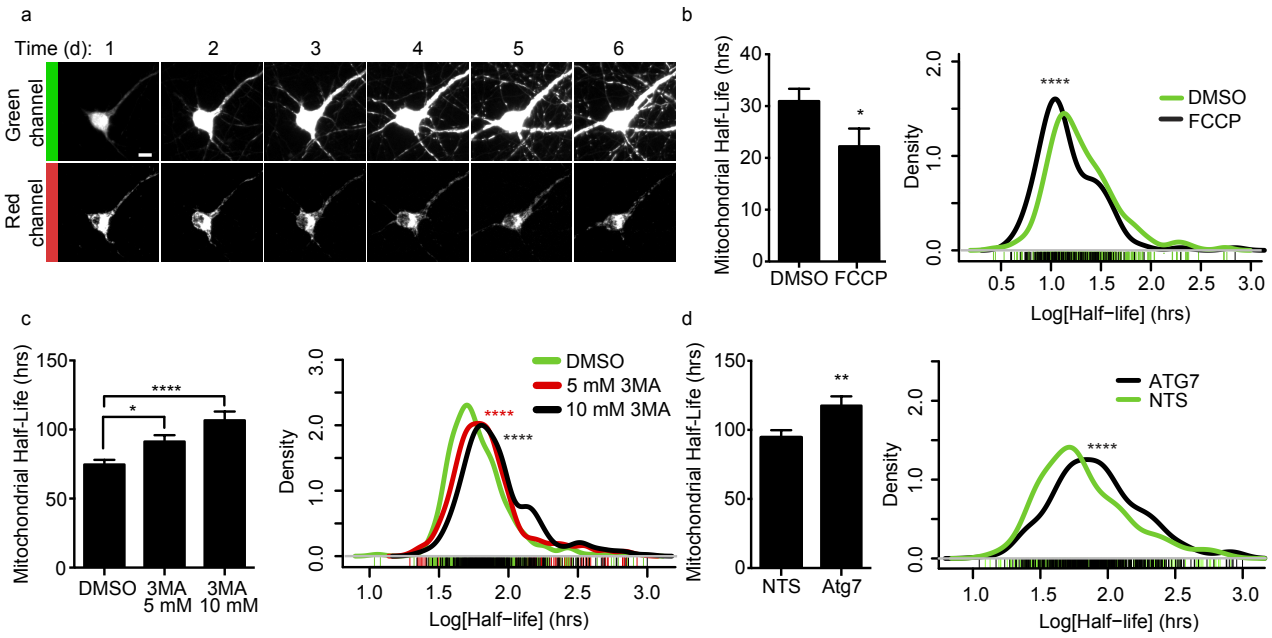


Figure 2.6 Characterization of a novel assay for mitochondrial autophagy in live neurons. (a) Expression of mitoEOS2 in primary cortical neurons. Primary neurons co-transfected with mitoEOS2 and EGFP were photoswitched and tracked over time using longitudinal RM. The top row of images represents the EGFP signal while the bottom row represents the photoswitched red mitoEOS2 signal. Scale bar, 10 μm. (b) Effect of FCCP on mitoEOS2 clearance. Treatment of primary neurons with 1 μM FCCP, an uncoupler, shortens mitochondrial half-life. The left panel shows mean half-lives and the right panel shows density plots of the same data. Hash marks below the curves represent half-life values of individual neurons. FCCP treatment causes both a significant decrease in the mean half-life and a significant leftward shift in the distribution towards shorter half-lives. (c) Effect of 3-MA on mitoEOS2 clearance. Treatment of primary neurons with 5 mM or 10 mM 3-MA, an inhibitor of autophagosome formation, lengthens mean mitochondrial half-life and significantly shifts the distribution of half-lives to the right. (d) Effect of Atg7 knockdown on mitoEOS2 clearance. Primary neurons were infected with lentivirus expressing a non-targeting shRNA (NTS) or an shRNA against Atg7. Atg7 shRNA expression lengthens mean mitochondrial half-life and significantly shifts the distribution of half-lives to the right. Means across conditions were compared using 1-way ANOVA with Dunnett's correction or Student's t-test. Distributions were compared using a Mann-Whitney-Wilcoxon test. *, p<0.05; **, p<0.01; ***, p<0.001; ****, p<0.0001

In addition to genetic manipulations of autophagy, we sought to manipulate mitophagy genetically in order to demonstrate that our assay can detect mitophagy induced by a variety of stimuli. The best-established pathway known to regulate mitophagy in mammalian cells is the PINK1-Parkin pathway (*38*), where Parkin-mediated phosphorylation of PINK1 targets mitochondria for degradation. In order to determine whether the assay could detect changes in mitophagy due to modulation of the PINK1-Parkin pathway, we cultured neurons from Parkin KO and Parkin WT rats and measured mitophagy as described above. We found that mean

mitochondrial half-life was slightly reduced (Fig. 2.7, left), and the half-life distribution was shifted to the left towards shorter half-lives (Fig. 2.7, right). The reduction in half-life we observed may be a consequence of a compensatory upregulation of mitophagy in the absence of Parkin.

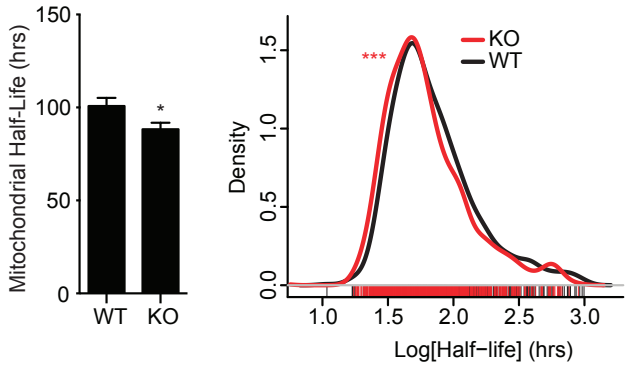


Figure 2.7 Effect of Parkin KO on mitophagy. Primary cortical neurons from PARK$^{+/+}$ (WT) and PARK$^{-/-}$ (KO) rats were cultured and mitophagy assayed as described above. Parkin KO resulted in a significant reduction in mean mitochondrial half-life (left) and significantly shifted the distribution of half-lives to the left (right). Means across conditions were compared using Student's t-test. Distributions were compared using a Mann-Whitney-Wilcoxon test. *, $p<0.05$; ***, $p<0.001$

Overall, we observed that the mitoEOS2 assay reported the predicted changes in mitochondrial half-life in response to defined manipulations of autophagy and mitophagy. We conclude that the mitoEOS2 assay is a valid and sensitive way to measure the rate of mitophagic flux and provides an approach to measure mitophagy at a single cell level.

2.4 CHARACTERIZATION OF BASAL MITOCHONDRIAL HALF-LIFE IN HEALTHY NEURONS

We next wondered whether rates of mitochondrial clearance vary among healthy primary neurons. We previously reported that the clearance rate of specific proteins in single cells varies

three- to fourfold across a population of neurons, indicating that the proteostasis machinery in individual neurons varies substantially (*85*). The mean half-life measured using this assay is ~100 hours. Surprisingly, however, mitochondrial half-life varied by as many as 2 orders of magnitude (10-1000 hours) (Fig. 2.3d). This unexpected diversity in mitochondrial turnover rates raises the intriguing possibility that substantial differences underlie the signals or machinery that govern mitophagy in individual neurons.

CHAPTER 3.
NEURONAL MITOPHAGY IS MODULATED BY HUNTINGTIN EXPRESSION AND PREDICTS NEURODEGENERATION

3.1 ESTABLISHMENT OF AN HD MODEL IN WHICH TO STUDY MITOPHAGY

We next sought to establish an HD model in which to study mitophagy and its relationship to mHtt expression, mitochondrial dysfunction, and neurodegeneration. We previously established a primary neuron model of HD involving overexpression of wild-type or mutant Htt^{ex1} tagged with fluorescent proteins to visualize expression levels and aggregation (*24*). This model recapitulates numerous features of human HD, including the abnormal aggregation of $mHtt^{ex1}$ into IBs and polyglutamine expansion-dependent neurodegeneration caused by mHtt (*29*). For this study, we established an HD model by expressing Htt^{ex1}-Q25-GFP (wild-type Htt) or Htt^{ex1}-Q97-GFP (mHtt) in primary cortical neurons. Survival was measured by tracking individual neurons with RM. Neurons were labeled as dead upon loss of fluorescence, which we previously established as a marker of cell death (*24*). Neurons expressing Htt^{ex1}-Q97-GFP survived less well, indicated by a higher cumulative risk of death (Fig. 3.1a), than those expressing Htt^{ex1}-Q25-GFP, consistent with our reports of polyQ expansion-mediated toxicity (*24*). In addition, mHtt frequently aggregated into IBs in neurons expressing Htt^{ex1}-Q97-GFP, whereas neurons expressing Htt^{ex1}-Q25-GFP never formed IBs (data not shown).

As mHtt is associated with mitochondrial damage (*72-74*, *97*), and mitochondrial damage triggers mitophagy (*77*), we investigated whether our HD model exhibited mitochondrial dysfunction. Levels of reactive oxygen species (ROS) in neurons are a key readout of mitochondrial dysfunction: inefficient mitochondrial respiration leads to increased ROS production (*98*). In addition, oxidative stress is implicated as a mechanism underlying multiple neurodegenerative diseases (*99*). To measure ROS levels, neurons expressing EBFP2-tagged Htt^{ex1}-Q25 or Htt^{ex1}-Q97 were treated with 5 μM CellROX Deep Red for 30 min. CellROX Deep

Red becomes fluorescent upon oxidation, and its fluorescence intensity increases proportionally to the levels of ROS in the cell. CellROX Deep Red fluorescence was significantly greater in neurons expressing Htt^{ex1}-Q97-EBFP2 compared with Htt^{ex1}-Q25-EBFP2 (Fig. 3.1b), indicating that mHtt induced mitochondrial dysfunction before neurodegeneration in this HD model.

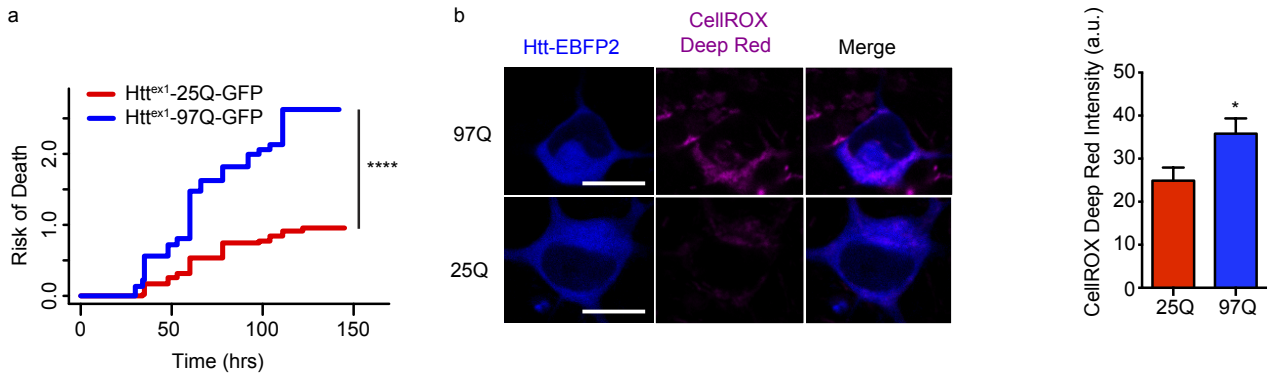


Figure 3.1 Mutant Htt induces neurodegeneration and mitochondrial dysfunction. (a) Survival analysis of neurons expressing Htt^{ex1}-25Q-GFP and Htt^{ex1}-97Q-GFP. Neurons expressing mutant (97Q) Htt^{ex1}-GFP have a higher risk of death than neurons expressing wild-type (25Q) Htt^{ex1}-GFP. (b) ROS levels in neurons expressing Htt^{ex1}-25Q-EBFP2 and Htt^{ex1}-97Q-EBFP2. CellROX Deep Red fluorescence is increased in the presence of Htt^{ex1}-97Q-EBFP2, indicating increased ROS levels. Neurons were treated with 5 μM CellROX Deep Red for 30 min. Scale bar, 10 μm. Survival curves were compared using a log-rank test. Means across conditions were compared using Student's t-test. *, p<0.05; ***, p<0.001; ****, p<0.0001

3.2 EVALUATION OF MITOCHONDRIAL FUNCTION IN THE HD MODEL

In addition to ROS, we also measured a number of other readouts of mitochondrial function including ATP production, mitochondrial mass, and mitochondrial membrane potential. ATP production was measured by transfecting neurons with a FRET-based ATP sensor (AT1.03) that measures ATP concentration in the cell via FRET readout (*100*). Mitochondrial mass was measured by staining Htt^{ex1}-expressing neurons with MitoTracker Green, and mitochondrial content was calculated as described in the Methods. Mitochondrial membrane potential was measured by staining neurons with tetramethylrhodamine methyl ester (TMRM), a dye whose fluorescence is high in normal mitochondria and low in depolarized mitochondria (*101*). All

neurons were transfected with Htt^{ex1}-Q97 or Htt^{ex1}-Q25 tagged with mCherry (for ATP experiment), EBFP2 (for mitochondrial mass experiment), or GFP (for TMRM experiment). No difference was observed in normalized FRET (NFRET) in neurons expressing wild-type or mHtt (Fig. 3.2a). In addition, no difference was observed in mitochondrial mass in neurons expressing wild-type or mHtt (Fig. 3.2b). However, neurons expressing mHtt actually had higher TMRM fluorescence compared to neurons expressing wild-type Htt (Fig. 3.2c). Overall, mitochondria in mHtt-expressing neurons seem to be producing ATP and maintaining their membrane potential similarly to mitochondria in wild-type Htt-expressing neurons. Validation of the ATP and TMRM assays can be found in the Appendix.

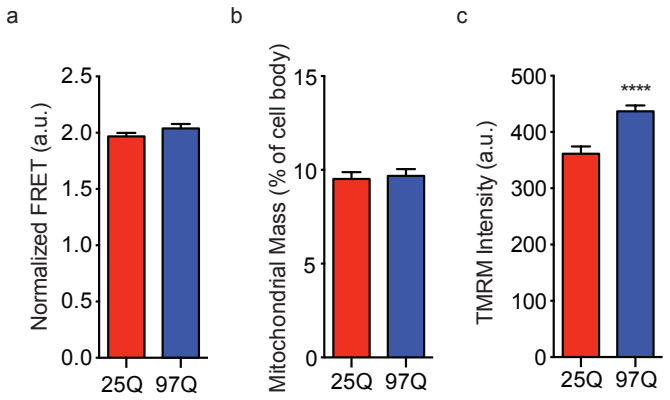


Figure 3.2 Mitochondrial function assessment in neurons expressing wild-type and mHtt. (a) ATP levels in neurons expressing Htt^{ex1}-Q25-mCherry or Htt^{ex1}-Q97-mCherry. ATP levels were assayed using a FRET-based ATP sensor. No difference in normalized FRET (NFRET) was observed between cells expressing wild-type and mHtt. (b) Mitochondrial mass in neurons expressing Htt^{ex1}-Q25-EBFP2 or Htt^{ex1}-Q97-EBFP2. Mitochondrial mass was assayed by reconstructing mitochondrial volume from MitoTracker Green staining. No difference was observed in mitochondrial mass between cells expressing wild-type and mHtt. (c) Mitochondrial membrane potential in neurons expressing Htt^{ex1}-Q25-GFP or Htt^{ex1}-Q97-GFP. Neurons were stained with TMRM to assay membrane potential. Neurons expressing mHtt had increased TMRM intensity, and increased membrane potential, compared to neurons exressing wild-type Htt. Means across conditions were compared using Student's t-test. ****, $p<0.0001$

In addition to mitochondrial function, we also assayed mitochondrial morphology in the presence of wild-type and mHtt. Fragmented mitochondria produce less ATP, are more depolarized, and are selectively targeted for mitophagy (*78*). Thus, mitochondrial morphology can also serve as a readout of mitochondrial function. We assayed mitochondrial morphology in two ways: by co-transfecting a mitochondrially targeted fluorescent protein (mitoGFP) with Htt^{ex1} constructs and using an automated image analysis paradigm to determine mitochondrial morphology, and by performing electron microscopy (EM) on neurons infected with lentivirus expressing wild-type or mHtt and then manually determining mitochondrial morphology.

For the fluorescence-based approach, primary neurons were co-transfected with mito-GFP, Htt^{ex1}-EBFP2 plasmids, and mApple as a morphology marker. Htt^{ex1}-Q97-EBFP2 was transfected at three different levels: 0.4 μg, 0.2 μg, and 0.1 μg. Htt^{ex1}-Q25-EBFP2 was transfected at 0.4 μg. Neurons were imaged 24 hours post-transfection and mitochondrial morphology was quantified as described in the Methods section. Four parameters of mitochondrial morphology were quantified: circularity, skeleton length, blob count (the number of mitochondria in a cell body), and aspect ratio. Lower transfection levels (0.1 μg and 0.2 μg) of Htt^{ex1}-Q97-EBFP2 increased the mitochondrial circularity index compared to Htt^{ex1}-Q25-EBFP2-expressing cells, indicating that mitochondria in these neurons were more elongated and less circular (a circularity index of 1 is perfectly circular) (Fig. 3.3a). Lower transfection levels of Htt^{ex1}-Q97-EBFP2 also increased mitochondrial skeleton length (Fig. 3.3b). There was no change in blob count across any of the conditions (Fig. 3.3c). Finally, expression of any level of Htt^{ex1}-Q97-EBFP2 increased the aspect ratio of mitochondria, again indicating increased elongation (an aspect ratio of 1 represents a perfect circle) (Fig. 3.3d).

For the EM-based approach, primary neurons were infected with lentivirus expressing Htt^{ex1}-Q97-GFP or Htt^{ex1}-Q25-GFP. Seven days post-infection, neurons were lysed and prepared for electron microscopy as described in the Methods. Images were taken at 13600×. Areas of the samples containing mitochondria were selectively chosen for imaging. Mitochondria present in the images were manually analyzed to measure area, circularity, perimeter, and % of all mitochondria that appeared swollen. Neurons infected with Htt^{ex1}-Q97-GFP-expressing virus had larger mitochondria than neurons infected with Htt^{ex1}-Q25-GFP-expressing virus in terms of total area (Fig. 3.3e) and perimeter (Fig. 3.3g). There was no change in circularity across the two conditions (Fig. 3.3f). Both conditions also had ~40% swollen mitochondria (Fig. 3.3h). Overall, both approaches indicated that mitochondria in mHtt-expressing neurons are not more fragmented; to the contrary, mitochondria in these cells are larger and more elongated.

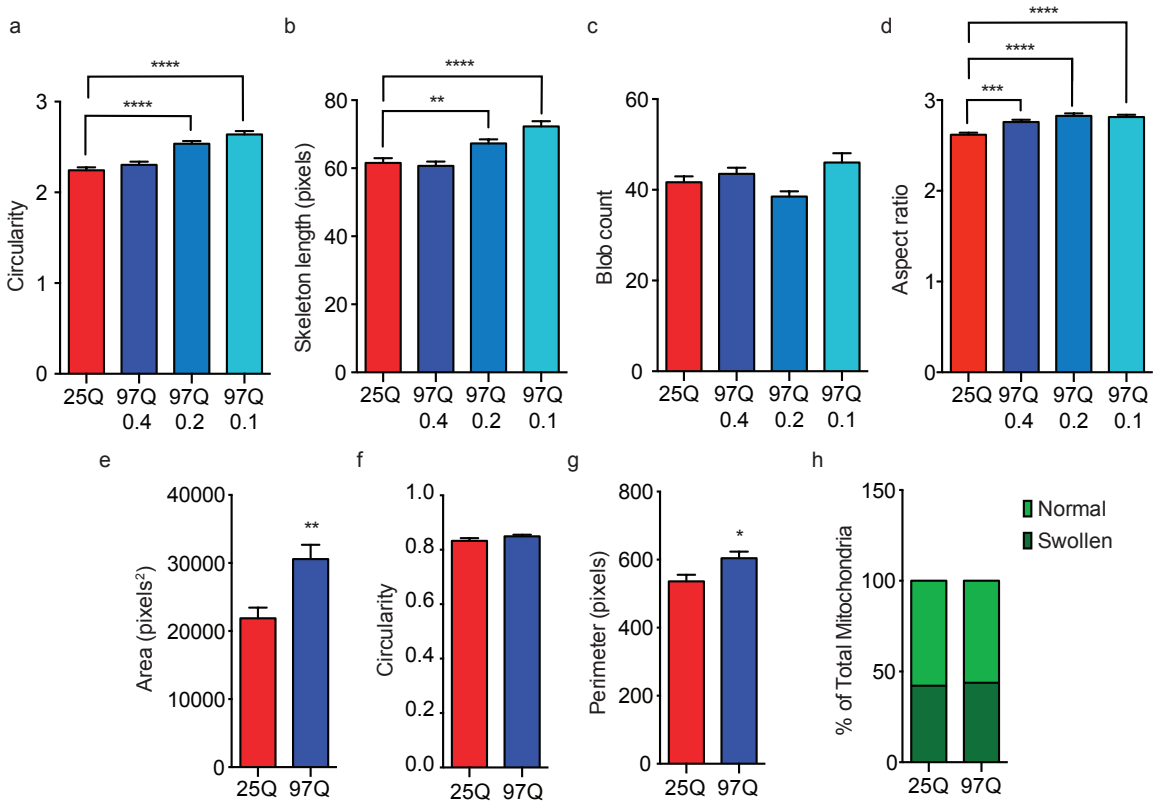


Figure 3.3 Assessment of mitochondrial morphology in neurons expressing wild-type and mHtt. (a-d) Neurons transfected with mito-GFP and EBFP2-tagged wild-type or mHtt were imaged and mitochondrial morphology assayed in an automated fashion as described above. mHtt was transfected at four different levels: 0.1 µg, 0.2 µg, and 0.4 µg. Four morphology parameters were assayed: mitochondrial circularity (a), skeleton length (b), blob count (c), and aspect ratio (d). (e-h) Neurons were infected with lentivirus expressing GFP-tagged wild-type or mHtt in the FUGW expression vector. 5 days after infection, neurons were prepared for EM imaging. Mitochondria present in EM images were assayed for area (e), circularity (f), perimeter (g), and degree of swollenness (h). Means across conditions were compared using 1-way ANOVA with Dunnett's correction or Student's t-test. *, p<0.05; **, p<0.01; ***, p<0.001; ****, p<0.0001

3.3 EVALUATION OF AUTOPHAGY RATES IN THE HD MODEL

Mitophagy is a cargo-specific form of general autophagy, possibly the only clearance pathway in cells that can clear aggregated protein. To further establish whether our HD model is suitable for investigating a relationship between mHtt and mitophagy, we first sought to demonstrate that we could detect an effect of mHtt on autophagy. We first asked whether the expression of mHtt induced an upregulation of autophagy. In order to assay autophagy, we first looked at overall

levels of LC3 in the cells. LC3 is the most specific known marker of autophagosomes, lining the inner and outer membranes, and is itself degraded by autophagy (*31*). Thus, its levels are related to the rate of autophagy in the cell. Neurons expressing Htt^{ex1}-Q25-EBFP2 or Htt^{ex1}-Q97-EBFP2 were stained with an antibody against LC3 and staining intensity was quantified. Htt^{ex1}-Q97-EBFP2-expressing neurons had a significant decrease in LC3 staining intensity, indicating a potential upregulation of autophagy leading to a reducing in total LC3 levels (Fig. 3.4a). However, as the LC3 stain is a snapshot-based measure, it does not distinguish between increased autophagy and reduced autophagosome synthesis. Thus, to complement this approach, we used an OPL LC3 clearance assay described previously (*89*) in neurons transfected with Htt^{ex1}-Q25-GFP or Htt^{ex1}-Q97-GFP. The half-life of LC3, as measured with the OPL assay, provides a single cell estimate of rates of autophagic flux (*89*). There was no change in the mean LC3 half-life with Htt^{ex1}-Q97-GFP (Fig. 3.4b, left). However, consistent with our previous findings (*85*), we found a modest but significant leftward shift in the distribution of LC3 half-lives in Htt^{ex1}-Q97-GFP-expressing neurons (Fig 3.4b, right), indicating shorter LC3 half-lives in this population and faster rates of autophagy. These findings indicate that neurons upregulate autophagy in response to Htt^{ex1}-Q97-GFP expression.

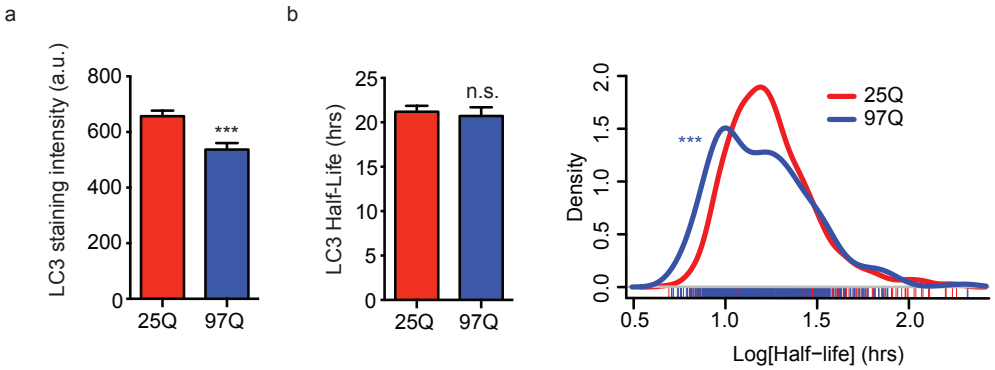


Fig 3.4 Mutant Htt increases autophagy. (a) Immunocytochemistry was performed on neurons transfected with Htt^{ex1}-Q25-EBFP2 or Htt^{ex1}-Q97-EBFP2 for LC3 levels. Neurons expressing mHtt had significantly lower LC3 levels than neurons expressing wild-type Htt. (b) Autophagy flux in neurons expressing Htt^{ex1}-25Q-GFP and Htt^{ex1}-97Q-GFP. Expression of Htt^{ex1}-97Q-GFP has no effect on mean LC3 half-life (left panel), but significantly shifts the distribution of LC3 half-lives to the left towards shorter half-lives (right panel), indicating an induction of autophagy. Survival curves were compared using a log-rank test. Distributions were compared using a Mann-Whitney-Wilcoxon test. ***, $p<0.001$

3.4 EFFECT OF MUTANT HTT EXPRESSION ON MITOCHONDRIAL HALF-LIFE IN AN UNSTRATIFIED POPULATION OF NEURONS

We next used our model to investigate whether mitophagy is altered with mHtt. We first evaluated whether lysosomal degradation of mitochondria is altered in neurons expressing mHtt by quantifying mitochondrial delivery to lysosomes with mito-mKeima (*102*). Keima emits green fluorescence (~447 nm) at neutral pH, but undergoes a spectral shift and emits red fluorescence (~561 nm) in acidic environments. By fusing a sequence that targets Keima to mitochondria, mt-mKeima, we can differentially image mitochondria in lysosomes and in the cytoplasm (Fig. 3.5a). The distributions of mitochondria in these compartments can be quantified by measuring the ratio of mt-mKeima fluorescence at 561 and 447 nm. A high ratio indicates that most mitochondria are in the acidic lysosomal compartment, while a low ratio indicates that most mitochondria are outside of the lysosome. As lysosomal degradation is the last step in mitophagy, co-localization of mitochondria with lysosomes is a measure of mitophagy (*103*).

Differing numbers of mitochondria co-localized with lysosomes in the presence of mHtt thus indicates a change in mitochondrial degradation via mitophagy.

To determine the effect of mHtt on the mt-mKeima fluorescence ratio, neurons co-transfected with EBFP2-tagged Htt^{ex1}-Q25 or Htt^{ex1}-Q97 and mt-mKeima were imaged and the 561 nm /447 nm fluorescence ratio quantified. Neurons expressing Htt^{ex1}-Q97-EBFP2 had a higher fluorescence index compared to neurons expressing Htt^{ex1}-Q25-EBFP2, indicating that mitophagy may be increased in the presence of mHtt in an unstratified population of neurons (Fig. 3.5b).

One potential limitation is that the mt-mKeima assay makes inferences about mitophagic flux based on steady-state changes in mitochondrial distributions between cytoplasmic and lysosomal compartments. An increase in mitochondrial localization to lysosomes reported by mt-mKeima might be caused by reduced lysosomal degradation rather than increased mitochondrial clearance. To overcome this limitation, we used the mitophagy assay we developed to directly measure mitochondrial clearance rates. Neurons co-transfected with Htt^{ex1}-Q25-GFP or Htt^{ex1}-Q97-GFP and mitoEOS2 (Fig. 3.5c) were photoconverted with 405-nm light and imaged at 12-hr intervals for 30−40 hours using robotic microscopy. Mitochondrial half-life was calculated as above. We found no significant difference in mean mitochondrial half-life (Fig. 3d, left) or the distributions of mitochondrial half-lives (Fig. 3.5d, right) in neurons expressing Htt^{ex1}-Q25-GFP and Htt^{ex1}-Q97-GFP. These data indicate that mHtt expression does not affect mitochondrial clearance through the mitophagy pathway in an unstratified population of neurons.

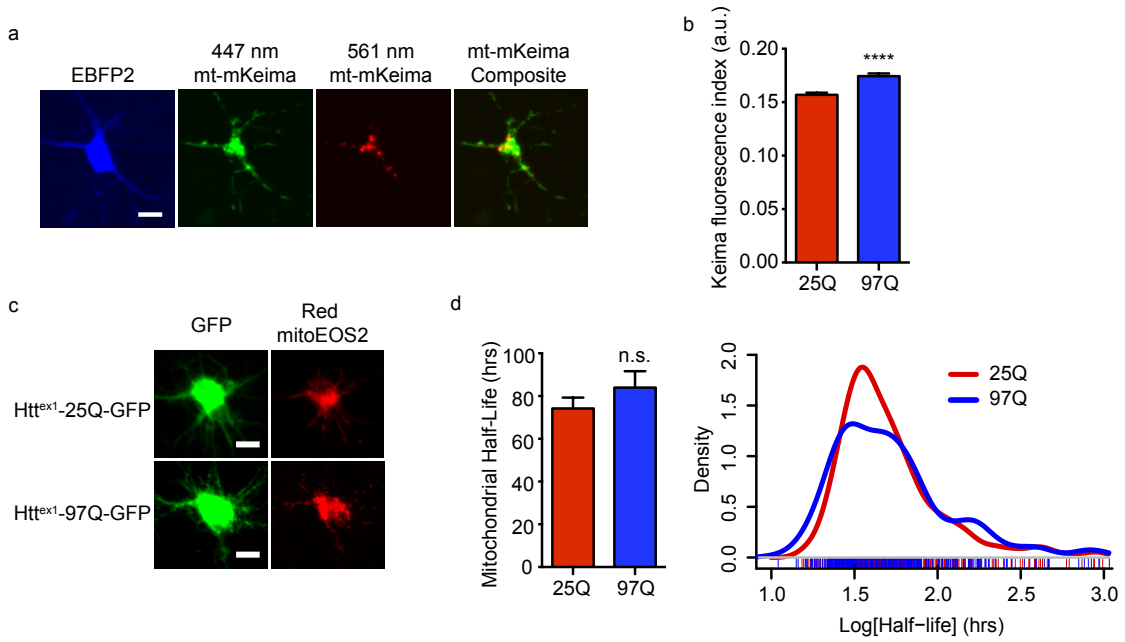


Figure 3.5. Effects of mutant Htt on mitochondrial localization to lysosomes and mitophagy. (a) Mt-mKeima expression in primary cortical neurons. Excitation with 447 nm produces an image of Keima-labeled mitochondria in the cytoplasm, while excitation with 561 nm produces an image of Keima-labeled mitochondria in lysosomes. Scale bar, 10 μm. (b) Mt-mKeima fluorescence index in neurons expressing Htt^{ex1}-25Q-EBFP2 and Htt^{ex1}-97Q-EBFP2. 97Q expression increases the mean mito-mKeima fluorescence index (ratio of 561 nm/447 nm fluorescence). (c) Co-expression of Htt^{ex1}-GFP constructs with photoswitched mitoEOS2. The left column represents the EGFP signal from the Htt^{ex1} plasmids while the right column represents the red (photoswitched) mitoEOS2 signal from the same cells. Scale bar, 10 μm. (d) Mitophagy flux in neurons expressing Htt^{ex1}-25Q-GFP and Htt^{ex1}-97Q-GFP. There is no difference in mean mitochondrial half-life or the distribution of mitochondrial half-lives across populations of neurons expressing Htt^{ex1}-25Q-GFP and Htt^{ex1}-97Q-GFP. Means across conditions were compared using Student's t-test. Distributions were compared using a Mann-Whitney-Wilcoxon test. ***, $p<0.001$

3.5 MITOCHONDRIAL CLEARANCE RATES IN NEURONS WITH AND WITHOUT INCLUSION BODIES

In our analysis, we treated each live neuron identically, whether mHtt had aggregated into an IB or not. However, IB formation is an adaptive response neurons mounted to mHtt that improves survival (*24*). Thus, a potential explanation for a failure to find an effect in a population of mHtt-expressing neurons may be due to the existence of two subpopulations of cells, one with IBs and one without, in which opposite effects are occurring and canceling each other out. To test this

idea, we first re-examined ROS levels in neurons with and without IBs. Neurons expressing EBFP2-tagged Htt^{ex1}-Q25 or Htt^{ex1}-Q97 were treated with CellROX Deep Red and imaged. We found that neurons with diffuse Htt^{ex1}-Q97-EBFP2 had increased CellROX Deep Red fluorescence compared with neurons expressing Htt^{ex1}-Q25-EBFP2 (Fig. 3.6a). However, ROS levels in neurons with Htt^{ex1}-Q97-EBFP2 IBs were not significantly different from neurons expressing Htt^{ex1}-Q25-EBFP2, indicating that the presence of an IB restores mitochondrial ROS production to wild-type levels. These data also supported the idea that neurons with IBs may be in a different functional state than similar neurons without IBs (*29*).

With this in mind, we considered whether mitochondrial localization and clearance were different in mHtt-expressing neurons with and without IBs. We first used the mt-mKeima fluorescence index to evaluate whether localization of mitochondria to lysosomes was altered in neurons with and without IBs**.** Diffuse Htt^{ex1}-Q97-EBFP2-expressing neurons had a higher fluorescence index than Htt^{ex1}-Q25-EBFP2-expressing neurons. Neurons with Htt^{ex1}-Q97-EBFP2 IBs, on the other hand, had a significantly lower fluorescence index than neurons with diffuse Htt^{ex1}-Q97-EBFP2, indicating a reduction in mitochondrial localization to lysosomes in the presence of mHtt IBs (Fig. 3.6b).

We then measured mitochondrial half-life in our OPL mitophagy assay to determine whether the increased localization of mitochondria to lysosomes in IB-containing neurons indicated a change in mitophagy flux. Indeed, neurons containing Htt^{ex1}-Q97-GFP IBs exhibited a longer mean mitochondrial half-life than neurons containing diffuse Htt^{ex1}-Q97-GFP or neurons expressing Htt^{ex1}-Q25-GFP (Fig. 3.6c, left). In addition, when we looked at the distributions of half-lives in

these populations, the presence of diffuse mHtt shifted the distribution significantly leftward towards shorter half-lives, while the presence of mHtt IBs shifted the distribution significantly rightwards towards longer half-lives (Fig. 3.6c, right). These data indicate that mitophagy flux in mHtt-expressing neurons depends on whether the neuron has formed an IB.

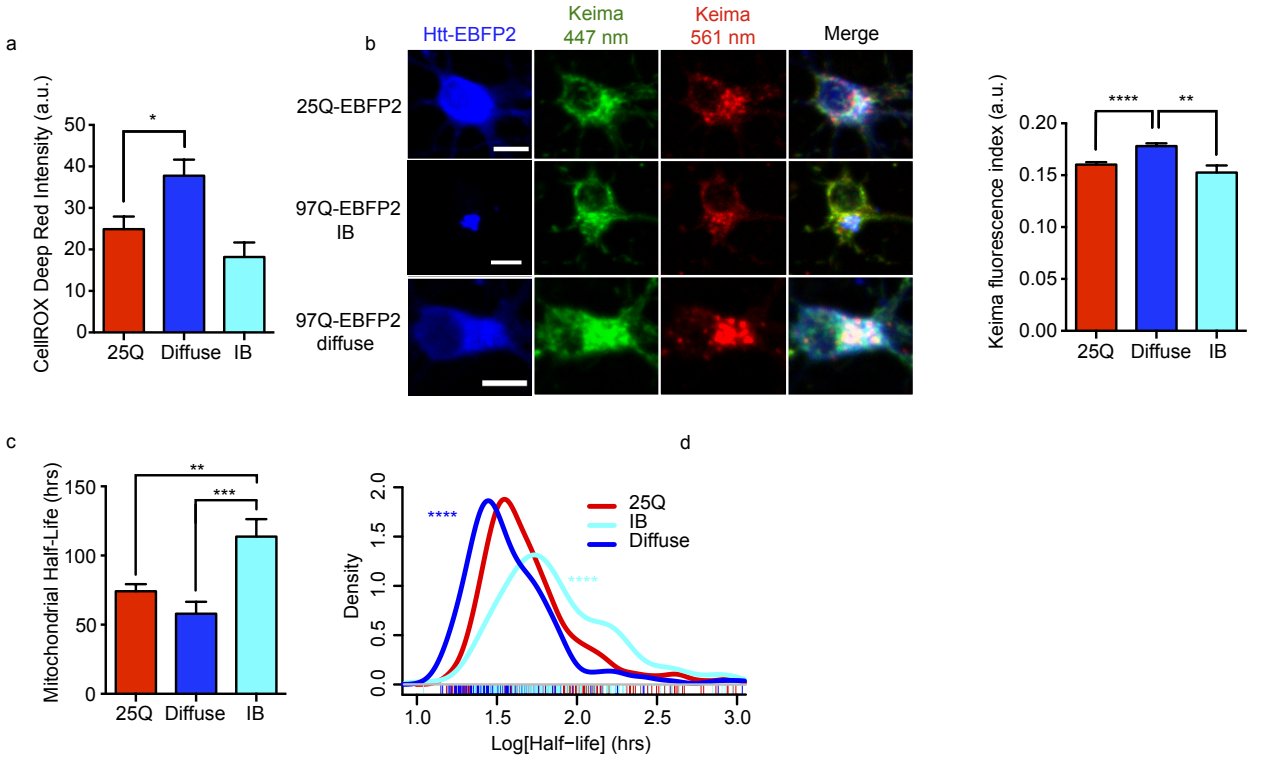


Figure 3.6 Mitochondrial clearance rates differ in neurons containing diffuse mHtt or IBs. (a) ROS levels in neurons with Htt^{ex1}-25Q-EBFP2 (“25Q”), diffuse Htt^{ex1}-97Q-EBFP2 (“Diffuse”), or Htt^{ex1}-97Q-EBFP2 that has formed an IB (“IB”). Neurons containing diffuse mHtt exhibited increased CellROX Deep Red fluorescence compared to wild-type Htt neurons. CellROX Deep Red levels in neurons with IBs did not differ from wild-type Htt neurons. (b) Mt-mKeima fluorescence index in neurons with Htt^{ex1}-25Q-EBFP2, diffuse Htt^{ex1}-97Q-EBFP2 or IB Htt^{ex1}-97Q-EBFP2. The fluorescence index is significantly reduced in neurons containing mHtt IBs compared to neurons containing diffuse mHtt. Representative images (left) and mean index per condition (right). (c) Mitophagy flux in neurons containing Htt^{ex1}-25Q-GFP, diffuse Htt^{ex1}-97Q-GFP or IB Htt^{ex1}-97Q-GFP. Neurons containing mHtt IBs exhibited increased mean mitochondrial half-life compared to both wild-type Htt neurons and diffuse mHtt neurons (left panel). In addition, neurons with diffuse mHtt expression significantly shifted the distribution of mitochondrial half-lives leftward, while IB formation significantly shifted the distribution of mitochondrial half-lives rightward (right panel). Means across conditions were compared using 1-way ANOVA with Tukey’s correction. Distributions were compared using a Mann-Whitney-Wilcoxon test. *, p<0.05; **, p<0.01; ***, p<0.001; ****, p<0.0001

3.6 AUTOPHAGY RATES IN NEURONS WITH AND WITHOUT INCLUSION BODIES

Do neurons that form IBs exhibit a change in autophagy flux analogous to the one observed for mitophagy? We first measured LC3 levels in neurons with and without IBs. Neurons with diffuse mHtt had lower levels of LC3 than wild type Htt-expressing neurons. However, neurons with IBs did not significantly differ in LC3 levels from wild type Htt-expressing neurons, indicating that autophagy is upregulated in neurons with diffuse mHtt but not IB mHtt (Fig. 3.7a). We also used the OPL LC3 assay described previously (*89*) to measure autophagic flux. We found that neurons with Htt^{ex1}-Q97-GFP IBs had a greater mean LC3 half-life than neurons containing diffuse Htt^{ex1}-Q97-GFP (Fig. 3.7b, left). Diffuse mHtt also shifted the distribution of LC3 half-lives leftward, while the presence of IBs shifted the distribution rightward (Fig 3.7b, right). Thus, both autophagy and mitophagy flux are accelerated in cells with diffuse mHtt and slowed in cells with IBs.

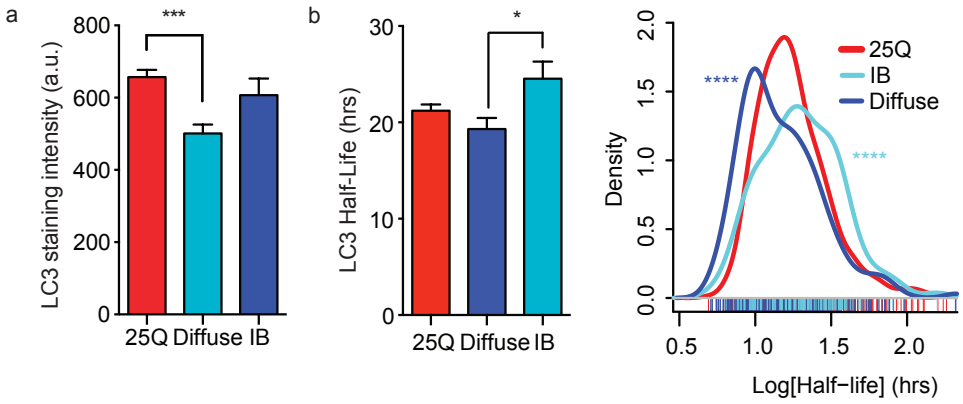


Fig 3.7 LC3 levels in neurons expressing wild-type or mHtt. (a) Immunocytochemistry was performed on neurons transfected with Htt^{ex1}-Q25-EBFP2 or Htt^{ex1}-Q97-EBFP2 for LC3 levels. Neurons expressing Htt^{ex1}-Q97-EBFP2 were broken down into cells that do or do not have IBs. Neurons with IBs had significantly lower LC3 levels than neurons expressing wild-type Htt. (b) Autophagy flux in neurons expressing Htt^{ex1}-25Q-GFP, diffuse Htt^{ex1}-97Q-GFP or IB Htt^{ex1}-97Q-GFP. Neurons containing mHtt IBs exhibited increased mean LC3 half-life compared to diffuse mHtt neurons (left panel). In addition, neurons with diffuse mHtt expression significantly shifted the distribution of LC3 half-lives leftward, while IB formation significantly shifted the distribution of LC3 half-lives rightward (right panel). Means across conditions were compared using 1-way ANOVA with Tukey's correction or Student's t-test. Distributions were compared using a Mann-Whitney-Wilcoxon test. *, p<0.05; ***, p<0.001; ****, p<0.0001

3.7 SEQUESTRATION OF AUTOPHAGY PROTEINS BY INCLUSION BODIES

What could be a potential mechanism for the slowing of autophagy and mitophagy in neurons with IBs? One potential explanation is that IBs sequester proteins that are necessary for autophagy, thus taking up autophagy capacity and reducing the degradation of other autophagic cargo, such as LC3 and mitochondria. IBs are known to co-localize with autophagy-related proteins such as p62, LC3, and optineurin (*104*, *105*). Optineurin and p62 are also necessary for mitophagy (*106*). In order to determine whether optineurin and p62 levels differed in neurons with and without IBs, neurons were co-transfected with mCherry-tagged Htt^{ex1}-Q97 constructs and GFP as a morphology marker. 60 hours post-transfection, neurons were fixed and stained with antibodies against p62 or optineurin. For cells containing IBs, optineurin and p62 levels

were assayed in the area of the cell body outside of the IB. In cells containing IBs, cytoplasmic p62 levels were significantly lower than in cells containing diffuse mHtt (Fig. 3.8a, left). P62 was also highly localized to the IB (Fig. 3.8a, right). Optineurin levels were not significantly different between cells containing IBs and cells containing diffuse mHtt, but there was a trend towards a reduction of optineurin in cells containing IBs (Fig. 3.8b). Although we did not test directly whether this level of sequestration would be expected to impact the autophagy or mitophagy rate, sequestration of autophagy-related proteins by mHtt IBs may contribute to the reduction of autophagy and mitophagy observed in these cells.

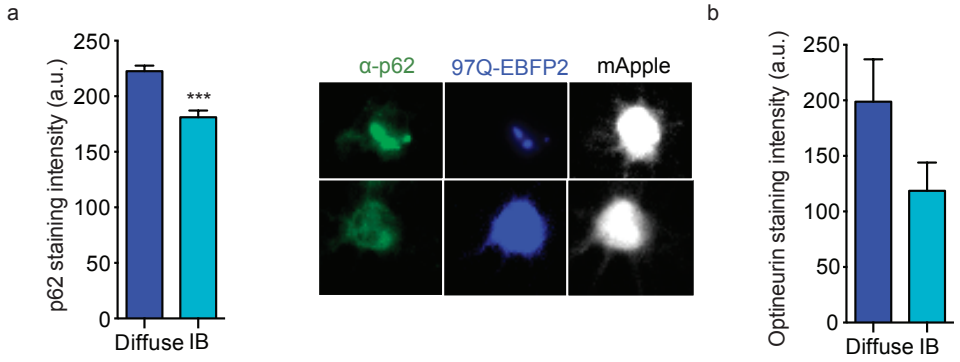


Fig 3.8 Levels of autophagy-related proteins in cells with and without IBs. (a) Levels of cytoplasmic p62 in neurons expressing Htt^{ex1}-Q97-EBFP2 that do or do not have IBs. p62 was measured in the cytoplasmic area that did not contain the IB. Neurons with mHtt IBs had significantly reduced levels of p62 protein compared to neurons with diffuse mHtt. (b) Levels of optineurin in neurons expressing Htt^{ex1}-Q97-EBFP2 that do or do not have IBs. Optineurin was measured in the cytoplasmic area that did not contain the IB. Neurons with mHtt IBs slightly reduced levels of optineurin protein compared to neurons with diffuse mHtt, but this trend did not reach significance. Means across conditions were compared using Student's t-test. ***, $p<0.001$

3.8 RELATIONSHIP BETWEEN MITOPHAGY RATES AND NEURONAL SURVIVAL

What is the underlying epistatic relationship among mHtt levels, IB formation, mitophagy, and survival? Experimentally, this is difficult to address directly because events, such as IB

formation and cell death, occur asynchronously across the whole cell population. Also, it is difficult to deduce the role of each variable experimentally because it is impossible to hold the others constant.

To overcome these limitations, we took advantage of advanced Bayesian statistical modeling and the unique datasets we generated with RM and dynamic repeated measures of all the critical variables. With Bayesian hierarchical approaches, we built a model that incorporated mHtt levels, IB formation, mitochondrial clearance, and survival as covariates, and regressed our data to determine the relationships that each variable has to the others. Bayesian modeling works by making initial predictions about relationships and then using data about each variable from each cell to refine the model, regressing the model to fit the actual data optimally. With conventional approaches using cross-sectional data, cell-to-cell variation in the levels of critical variables (e.g., mHtt levels, mitophagy rates) and the timing of key events (e.g., IB formation, cell death) would necessarily be averaged, obscuring the relationships. However, by observing these variables dynamically in individual cells, the variation is exploited by the Bayesian modeling to uncover underlying dose- and time-dependent relationships among the variables. The approach is also unbiased, and information from every cell is utilized to the fullest, whether a particular cell exhibits some of the features (e.g., IB formation, cell death) or not. This approach provides a way to disentangle the contribution of two variables to a future fate that might otherwise be linked by alternatively removing each variable from the model and comparing the effect on the predictions of the model.

To start, we focused on understanding these relationships in neurons expressing mHtt. IB formation is strongly dependent on mHtt levels; the probability of future IB formation rose significantly as mHtt levels rose (*29*). Higher mHtt levels also predicted shorter cell survival, and IB formation led to an abrupt reduction in levels of mHtt elsewhere in the cell and predicted better survival (*24*). Are these previous relationships discovered with less sophisticated statistical approaches replicated using more powerful Bayesian hierarchical modeling? We constructed a Bayesian regression model that integrates measures of mitochondrial clearance, mHtt expression, and IB formation and estimates the effect of each covariate on neuronal longevity in mHtt-expressing neurons. Initial Htt^{ex1}-Q97-GFP levels were a strong predictor of cell death, and IB formation was a strong predictor of neuronal survival, as reported previously (Fig. 3.9a).

Interestingly, the model revealed that mitochondrial clearance was a negative predictor of neuronal survival (Fig. 3.9a). Neurons with higher rates of mitochondrial clearance survived less well than those with lower rates.

As we previously observed that neurons with IBs exhibited slower mitochondrial clearance than neurons with diffuse mHtt, and have previously shown that high mHtt levels induce IB formation (*29*), we next investigated whether IB formation itself, or the total load of mHtt, was a stronger determinant of mitochondrial clearance rates. With Bayesian approaches, we can alternately remove each variable from the model and test the effect on its predictions. If the predictions are significantly different after variable removal, then a relationship exists (*107*). Therefore, we ran the regression model in three ways, including all three covariates (expression, IB formation, and decay), excluding IB formation, and excluding decay. Mean values of the effect of each

covariate on neuronal survival are shown in Table 3.1. When the IB formation covariate was removed, the predictive role of mitochondrial clearance and mHtt expression for neurodegeneration persisted, indicating that there is no evidence for a causal relationship between IB formation and mitochondrial clearance. By contrast, removing mHtt expression caused predictions to flip such that faster mitochondrial clearance predicted better survival, indicating a strong causal relationship between mHtt expression and mitochondrial clearance. Indeed, the correlation between mitochondrial decay and mHtt expression is strongly negative (Fig. 3.9d). Taken together, the model indicates that mHtt levels drive IB formation and reduce mitochondrial clearance rates and that there is no direct effect of IB formation on mitochondrial clearance.

Table 3.1 Bayesian regression analysis of the effects of mHtt expression level, IB formation, and mitochondrial clearance on neuronal survival

	mHtt expression	**IB formation**	**Mitochondrial clearance**
All covariates	0.341 (0.261−0.423),****	-0.138 (-0.284−0.0166),*	0.280 (0.0133−0.552),*
Without IB formation	0.345 (0.263−0.426),****	----	0.318 (0.082−0.576),**
Without mHtt expression	----	-0.157 (-0.310−0.00545),*	-0.133 (-0.377−0.0991),#

Table 3.1 Bayesian regression analysis of the effects of mHtt expression level, IB formation, and mitochondrial clearance on neuronal survival. Numbers represent the mean of the posterior probability distribution for the effect of each covariate on neuronal survival. A mean greater than zero indicates that the covariate is associated with reduced survival, while a mean smaller than zero indicates that the covariate is associated with improved survival. Analysis was performed including all covariate (first row), expression and decay only (second row), and IB formation and decay only (third row). 95% credible intervals are in parentheses. The probability that each distribution is different from zero is represented by asterisks. ****, P is not distinguishable from zero; **, $P < 0.01$; *, $P < 0.05$; #, $P=0.137$

Wild-type Htt may normally be critical in autophagy, including a role for the N-terminus of Htt used in these studies (*55*). This raises the intriguing possibility that at least part of the effect of Htt levels on mitophagy shown here might stem from a direct role of Htt on autophagy and mitophagy. To investigate this possibility further, we built Bayesian models from longitudinal single-cell data of neurons expressing GFP alone or Htt^{ex1}-Q25-GFP, in which expression levels, mitochondrial clearance rates and survival were determined. In neurons expressing GFP alone, higher mitochondrial clearance rates predicted better survival, and higher GFP expression correlated with an increased rate of mitochondrial clearance (Fig. 3.9c,f). These data indicate that mitochondrial decay in normal cells is a marker for improved neuronal survival. In neurons expressing Htt^{ex1}-Q25-GFP, on the other hand, higher mitochondrial clearance rates predicted worse survival, and higher Htt^{ex1}-Q25-GFP levels correlated with slower mitochondrial decay (Fig. 3.9b,e). Overall, the presence of Htt induces mitochondrial clearance, which is associated with increased toxicity. However, as mHtt and wild-type Htt levels go up, mitochondrial clearance decreases, potentially as a compensatory mechanism to prevent further cell death. As we found these effects in neurons expressing both wild-type and mHtt, it is likely that an intrinsic function or property of Htt is responsible for the effect of Htt on mitochondrial clearance.

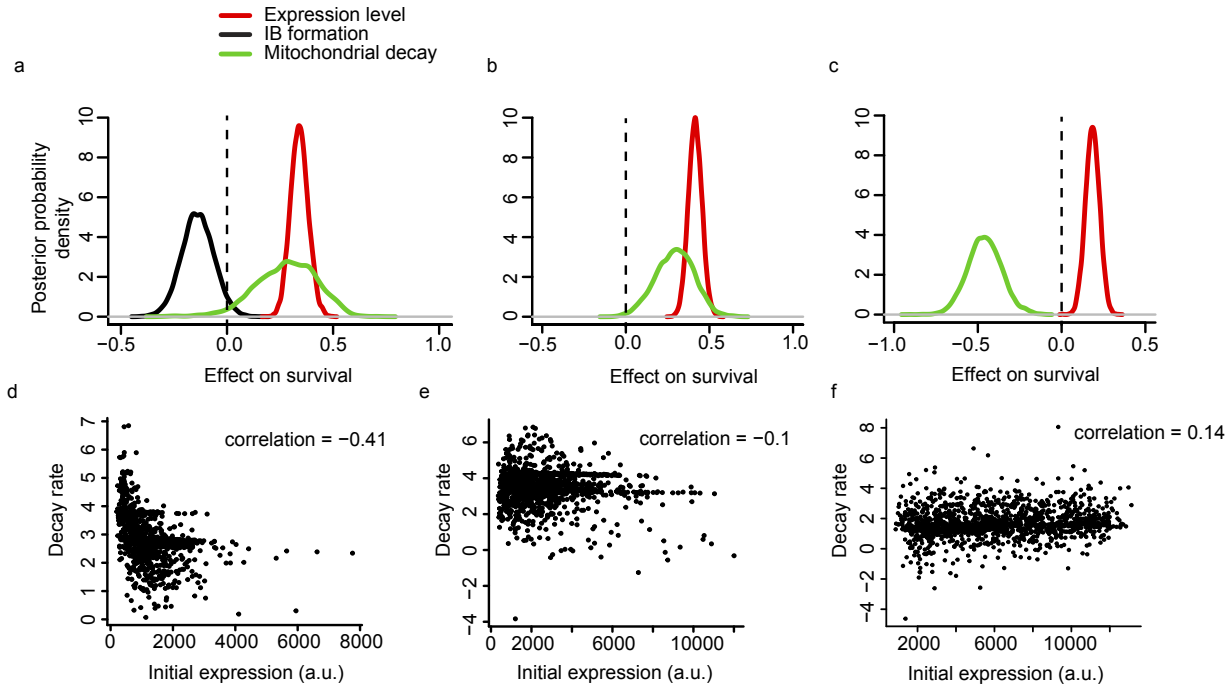


Figure 3.9 Mitochondrial clearance determines neurodegeneration. (a) Effect of IB formation, mHtt expression, and mitochondrial decay on mHtt-expressing neuronal longevity. The probability density for IB formation is clustered to the left of '0', indicating that IB formation reduces neuronal death. By contrast, the probability density for the initial levels of Htt^{ex1}-97Q-GFP is clustered to the right of '0', indicating that the larger the level of Htt^{ex1}-97Q-GFP, the sooner neurons die. The density for mitochondrial decay is also clustered to the right of '0', indicating faster mitochondrial decay is also associated with increased neuronal death. (b) Effect of wtHtt expression and mitochondrial decay on wtHtt-expressing neuronal longevity. In neurons expressing Htt^{ex1}-25Q-GFP, both increasing mitochondrial decay and initial levels are associated with increased neuronal death. (c) Effect of GFP expression and mitochondrial decay on GFP-expressing neuronal longevity. In neurons expressing GFP alone, increasing mitochondrial decay is associated with reduced neuronal death, while increased initial GFP expression is associated with slightly increased neuronal death. (d-f) Correlation between mitochondrial decay rate and Htt or GFP expression in neurons expressing Htt^{ex1}-97Q-GFP (d), Htt^{ex1}-25Q-GFP (e), and GFP (f). The probability that correlations are different from zero is not distinguishable from zero (d), 0.021 (e), and not distinguishable from zero (f).

CHAPTER 4.

MATERIALS AND METHODS

4.1 PLASMIDS

pGW1-GFP was described previously (*108*). Expression plasmids encoding an N-terminal fragment of Htt fused to GFP (pGW1- Htt^{ex1}-[Q25, Q97]-GFP) were derived as described previously (*24*, *29*). pGW1-EBFP2 was generated by subcloning EBFP2 from pBAD-EBFP2 (Addgene) into pGW1. EBFP2-tagged expression plasmids were generated by swapping GFP for EBFP2. pGW1-mCherry was described previously (*67*). pGW1-Htt^{ex1}-[Q25, Q97]-mCherry constructs were generated by subcloning Htt^{ex1}-[Q25,Q97] from pGW1-Htt^{ex1}-[Q25,Q97]-EGFP into pGW1 mCherry. pGW1-mito-mKeima was cloned into pGW1 from pIND-mt-mKeima (a generous gift of Dr. Atsushi Miyawaki). pGW1-mitoEOS2 was cloned into pGW1 from pEOS2-mito (a generous gift of Dr. Jayanta Debnath). pGW1 EOS2-LC3 was subcloned from pGW1 Dendra2-LC3, which was described previously (*89*). FUGW-Htt^{ex1} plasmids were generated by subcloning Htt^{ex1}-[Q25,Q97] from pGW1-Htt^{ex1}-[Q25,Q97]-EGFP into FUGW. FUGW-Atg[5,7,12] shRNA or FUGW-NTS plasmids were generated by subcloning the hU6 promoter and hairpin sequences from original pLK0.1 vectors. pCAGGS-AT1.03 was a generous gift from Dr. Ken Nakamura and originally described in Imamura et al., 2009 (*100*). pCAGGS-mitoGFP was a generous gift from Dr. Ken Nakamura.

4.2 shRNA

Atg7 shRNA (TRCN0000092163), Atg5 shRNA (TRCN0000327377), Atg12 shRNA (TRCN0000246729) and non-targeting shRNA (SHC002) pLK0.1 plasmids were obtained from Sigma.

4.3 LENTIVIRUS PRODUCTION

HEK293 cells at passage number <10 were grown to 80% confluence in 10 cm dishes coated with poly-D-lysine (EMD Millipore). Cells were transfected with empty FUGW or FUGW vectors expressing Htt^{ex1}-25Q or Htt^{ex1}-97Q, along with VSVG and Δ8.9 plasmids. Lipofectamine 2000 was used for transfections according to manufacturer's instructions. 48-96 hours after transfection, media was harvested, filtered with a 0.2 μm filter, combined with 5x PEG-It (System Biosciences), and stored at 4°C for 24-48 hours. Virus-containing media was then spun down for 30 min at 1500g at 4°C, the majority of the supernatant was removed, and remaining media was re-spun for 15 min at 1500g at 4°C. Virus pellets were then re-suspended in PBS. Virus was titered by quantifying the percentage of GFP-positive cells in an infected primary neuron culture.

4.4 PHARMACOLOGY

CCCP, FCCP, antimycin A, oligomycin, rotenone, and 3-MA were purchased from Sigma.

4.5 PRIMARY NEURON CULTURE

Primary rat cortical neurons were prepared from rat pup cortices at embryonic days (E)20 –E21 and cultured in Neurobasal media with B-27, Glutamax, and penicillin/streptomycin (NBM). Euthanasia for these experiments is entirely consistent with the recommendations of the Guidelines on Euthanasia of the American Veterinary Medical Association. For automated microscopy experiments, neurons were seeded at 1 x 10^6 cells per well on 96-well TPP® plates (Sigma) or CCB® plates (Perkin-Elmer). For confocal imaging experiments, neurons were seeded at the same density on 96-well glass-bottom dishes with #1.5 glass thickness (Mat-Tek). All plates were coated with poly-D-lysine (EMD Millipore) at 50 ug/ul and laminin at 5 ug/ul

(BD Biosciences) prior to neuron plating. At 4 d in vitro (DIV) neurons were transfected with plasmids by Lipofectamine 2000 (Invitrogen). All of the transfections involved 0.5 µl Lipofectamine 2000 per well. Cells were incubated with Lipofectamine–DNA complexes for no more than 1 hour at 37°C before rinsing. The remainder of the transfection protocol was per the manufacturer's suggestions.

4.6 IMMUNOCYTOCHEMISTRY

Primary rat cortical neurons were grown on 96-well plates. Neurons were transfected at 4 DIV. At 72 h post-transfection, immunocytochemistry was performed as described (*21*) and labeled with one of the following, anti-p62 (1:200, Progen), anti-LC3 (1:200, Novus) or anti-optineurin (1:200, Abcam). Primary antibody staining was followed by secondary antibody staining with either anti-guinea pig Alexa 647 (1:1000), anti-rabbit Alexa 488 (1:1000) or anti-rabbit Alexa 647 (1:1000) (Invitrogen).

4.7 QUANTITATIVE PCR WITH REVERSE TRANSCRIPTION

Primary rodent cortical neurons cultured as described above were rinsed in ice-cold PBS, and RNA was collected with the RNeasy kit (Qiagen). Equal amounts of RNA were used to generate cDNA from each replicate with the Applied Biosystems kit. SYBR Green (Applied Biosystems). Quantitect primer assays for actin and Atg7 (Qiagen) were used with a 7900HT Fast Real-Time PCR system. Each reaction was performed in duplicate and averaged. The Ct method was used to measure the effects of shRNA knockdown. To compare between replicates, each control sample was normalized to 1.

4.8 MITOCHONDRIAL FUNCTION ASSESSMENTS

Primary rat cortical neurons transfected with Htt^{ex1} plasmids and a morphology marker were treated with MitoTracker Green (100 nM), LysoTracker Deep Red (75 nM), TMRM (10 nM), MitoSox Red (1 μM), CellROX Deep Red (5 μM) (all from Life Technologies), or MitoView 633 (100 nM) (Biotium). All treatments were performed for 30 min at 37°C. Afterwards, cells were rinsed 4x with warm NBM or HBS (274 mM NaCl, 10 mM KCl, 1.4 mM Na_2HPO_4, 15 mM glucose, 42 mM HEPES) and imaged. For mitochondrial morphology assessment, primary rat cortical neurons were transfected with mito-GFP, Htt^{ex1} plasmids and a morphology marker.

4.9 ELECTRON MICROSCOPY

Cortical neurons were cultured as described above and infected with FUGW-Htt^{ex1}-[25Q,97Q] at 1 DIV. 5 days later, cultures were fixed in an ice-cold solution of 2% glutaraldehyde, 1% paraformaldehyde, and 100 mM sodium cacodylate (pH 7.4), postfixed in 2% osmium tetroxide, block-stained in 2% aqueous uranyl acetate, dehydrated in acetone, and embedded in LX-112 resin (Ladd Research Industries). Ultrathin sections were contrast-stained with 0.8% lead citrate, examined with a JEM-1230 electron microscope (JEOL USA), and photographed with an Ultrascan USC1000 digital camera (Gatan). Neurons were fixed and analyzed in an unbiased manner (i.e., every section of the cell has an equal probability of inclusion in the analysis). Mitochondria were identified as double-membrane structures with obvious cristae.

4.10 CONFOCAL MICROSCOPY

For mitochondrial function assessments, images were obtained with an inverted microscope (Nikon Ti-E) equipped with a Plan Apo VC 60×/1.4 Oil objective, Yokogawa CSU-22 spinning

disk confocal scanner, and a Photometrics Evolve Delta EMCCD camera. All components were encased in an Okolab environmental chamber kept at 37°C and 5% CO_2. Images were acquired using 405, 488, 561, and 640 nm lasers. The microscope was controlled using μManager software. 10-20 z-slices at a 0.25 μm interval were collected per neuron. Z-stacks were transformed into a maximum projection image and intensity information was extracted using ImageJ.

For mt-mKeima experiments, images were obtained using a TI Eclipse with a Yokogawa CSU-W1 spinning disk confocal scanner with a 20× Plan Fluor S 0.45NA ELWD objective and an Andor Zyla4.2 camera. Images were acquired using 445 and 561 nm lasers. All components were encased in a custom-designed Okolab environmental chamber kept at 37°C and 5% CO_2. The microscope was controlled using μManager software. A z-stack of images of 3 images at a 1 μM intervals was obtained for each well. This stack was transformed into a maximum projection image and intensity information was extracted using ImageJ.

Images used for mitochondrial morphology assessment were taken on the same system as those for the mt-mKeima experiments. Images were acquired using a 488 nm laser. A 40× Plan Fluor S 0.6NA ELWD objective was used for image acquisition. A z-stack of 5 images at 1 μm intervals was obtained for each well. This stack was transformed into a maximum projection image and intensity information was extracted using ImageJ.

4.11 AUTOMATED FLUORESCENCE MICROSCOPY

Experiments involving neuronal survival analysis and optical pulse imaging used an automated microscopy platform as described (*89*). Briefly, images were obtained with an inverted microscope (Nikon TE2000) equipped with the PerfectFocus system, a 20× Plan Fluor S 0.45NA ELWD objective and a 16-bit Andor Clara digital camera with a cooled charge-coupled device. Illumination was provided by a Lambda XL Xenon lamp (Sutter). All of the components were encased in a custom-designed, climate-controlled environmental chamber (InVivo Scientific), kept at 37°C and 5% CO2. The Semrock BrightLine full-multiband filter set (DAPI, FITC, TRITC, Cy5) was used for fluorophore photoactivation (DAPI), excitation and detection (FITC, TRITC). The illumination, filter wheels, focusing, stage movements and image acquisitions were fully automated and coordinated with publicly available (ImageJ and μManager) software.

4.12 IMAGE ANALYSIS

Relevant data were extracted from the raw, digital images in a sequential process using an original script developed in PipelinePilot (Accelrys, San Diego, CA). Briefly, the median background fluorescence from a portion of all images was calculated and subtracted from each individual image. The images were then assembled into montages representing each well at each time point. The montages were sequenced and aligned automatically, and neuron cell bodies were segmented on the basis of intensity and morphology. Among the variables recorded for each neuron were the fluorescence intensity and the time of death, marked by the loss of cellular fluorescence, rounding or dissolution of the cell body. Neurons with photoswitched mitoEOS2 values below 10 a.u. were excluded from half-life analyses. Statistical analyses and the generation of cumulative hazard plots and density plots were accomplished using custom-

designed algorithms and the survival package within R, while scatter plots and bar graphs were created using Prism (GraphPad).

4.13 SURVIVAL ANALYSIS

With longitudinal single cell data collected by tracking individual neurons over time, survival analysis was used to accurately determine differences in longevity between populations of cells (*109*). For longitudinal survival analysis, the survival time of a neuron was defined as the time point at which a cell was last seen alive. The survival package in R was used to construct Kaplan-Meier curves from the survival data. Survival functions were fitted to these curves and used to derive cumulative hazard (or risk-of-death) curves that describe the instantaneous risk-of-death for individual neurons in the cohort being tracked. Differences in the cumulative risk-of-death curves were assessed with the log rank test. We used Cox proportional hazards regression analysis (Cox analysis) to generate hazard ratios that quantified the relative risk-of-death between two cohorts of neurons or the predictive values of variables such as the presence of mHtt, changes in Htt levels or IB formation on the risk-of-death (*29*, *110*). The sign and size of the coefficient of the cellular feature describe, respectively, its predictive relationship to the fate of the cell and the magnitude of its effect. Hazard ratios and their respective *p* values were generated using the *coxph* function in the survival package for R statistical software (*111*). All Cox models were analyzed for violations of proportional hazards and for outlier data points using the *cox.zph* function in R.

4.14 MITOCHONDRIAL MORPHOLOGY ANALYSIS

Images of neurons transfected with mito-GFP and various Htt constructs were background subtracted and mitochondria were segmented based on the multi-scale vesselness filter followed by a multi-threshold segmentation and morphological analysis in ImageJ. The detection of linear or ridge-like structures was achieved using the property that the eigenvalues of the Hessian matrix may be used to determine the likelihood that a ridge-like structure is present. The vesselness metric was calculated at multiple scales for a given image by varying the σ of the Gaussian, thus giving a multi-scale approach for detecting ridges or vessels in an image. The final vesselness metric was obtained as follows,

$$\mathcal{V}_o(\gamma) = \max_{\sigma_{min} \leq \sigma \leq \sigma_{max}} \mathcal{V}_o(\sigma, \gamma)$$

where σ_{min} and σ_{max} are the minimum and maximum scales required to detect objects of the desired size. In the detection of mitochondria in 20× and 40× images, we set $\sigma_{min}=1$ and $\sigma_{max}=2$, with a step size of 0.1 giving us 10 scales at which the filters are evaluated. Ten thresholds for the vesselness images of each neuron were chosen and these threshold values were used to binarize the image. Small regions (typically with fewer than 3 pixels) were considered noise and removed using a morphological opening procedure. The cleaned, segmented image now contained regions that correspond to mitochondria and it was now possible to calculate various morphological characteristics at each threshold. The morphological properties calculated for quantification were eccentricity, circularity, ratio of major to minor axis of an ellipse fitted to each object (aspect ratio), skeleton length and area of each object. These were calculated at each threshold.

In addition to the morphological characteristics, the number of mitochondria per neuron were quantified through the use of a multi-scale blob detector based on the Laplacian of Gaussian (LoG) filter (*112*, *113*). Given a 2D Gaussian with variance

$$G(x, y; \sigma) = \frac{1}{\sqrt{2\pi\sigma^2}} e^{-\frac{x^2+x^2}{2\sigma^2}}$$

By applying the Laplacian operator to the Gaussian and convolving the Laplacian of Gaussian (LoG) obtained in this manner with the original image, regions of intensities greater than the local neighborhood were identified. With increasing scale (σ), the filter response attained a local maximum when the σ matched the feature size of interest. By applying the LoG filter at multiple scales, an estimate of the feature size and location was obtained by examining maxima in the scale space response.

4.15 MITOCHONDRIAL MASS ANALYSIS

Mitochondrial content was computed by image analysis using Fiji (*114*) and resulting data was processed in R. 3D image stacks of primary neurons were acquired on a spinning disk confocal microscope as described above for mitochondrial function experiments. Cells were transfected with Htt^{ex1}-EBFP2 constructs, pGW1-mApple as a morphology marker, and mitochondria were labeled with MitoTracker Green. Signals from the markers for neuronal morphology (mApple) and mitochondria (MitoTracker Green) were quantile normalized to compensate for different intensity ranges of the fluorophores and instrument biases. Automatic thresholding was applied on both channels using the method described by Huang and Wang (*115*) and implemented in Fiji. Resulting image masks were dilated once and remaining holes were closed. For the cell morphology marker, this led to uniform coverage of the cell area.

Masked pixels were counted in both channels for each slice and the ratio of the aggregated counts yielded an estimate of mitochondrial content for each 3D image stack.

4.16 BAYESIAN REGRESSION ANALYSIS

Because standard software is unable to accommodate the unique features of our data, we specify a hierarchical Bayesian model for our analysis. We build a proportional hazards model for cell survival times, where the hazard function is modulated by the covariates, which in our case include the initial expression of htt (denoted as X_1), the decay rate of red mitoEOS2 fluorescence (denoted as X_2), and the (time-dependent) presence or absence of an inclusion body (denoted as $X_3(t)$). The core model for the hazard, or instantaneous risk of death, for each cell i is, as a function of time,

$$h_i(t) = h_0(t) \exp\{\beta_0 + \beta_1 X_{1i} + \beta_2 X_{2i} + \beta_3 X_{3i}\}.$$

Several choices for the baseline hazard function $h_0(t)$ are available, including very flexible semiparametric specifications. For our data, exploratory analysis suggested that $h_0(t) = rt^{r-1}$, corresponding to a Weibull survival model, is adequate to fit our data well, for some unknown parameter r. Since the automated microscope images the cells at time intervals that are fairly wide relative to the length of the observation period, it is important that we account for the uncertainty in the times of death by modeling the survival times as interval censored (or right censored, if they live past the observation period), rather than known.

Furthermore, decay rates X_2 are not directly observable, so they are included in the model as unknown parameters as well. Specifically, since red mitoEOS2 fluorescence decays

approximately exponentially, we use a linear model for the log of red mitoEOS2 fluorescence as a function of time. That is, if Y_{ij} is the log of red mitoEOS2 fluorescence measured for cell i at time t_j , then

$$Y_{ij} = \beta_{0i} + \beta_{1i} t_j + \varepsilon_i ,$$

where the ε_i are normally-distributed errors. The decay rate for each cell i is then just the negative of the slope β_{1i} in the above equation. Random effects were included to account for differences among the four separate experimental runs that were analyzed. Because the regression model for the decay of red mitoEOS2 fluorescence is embedded within the hierarchical Bayesian model for cell survival, all of the error arising from estimating the decay rate is properly propagated into the final estimates of parameters in the survival model.

Finally, again as a result of the widely-spaced observation times, the time until inclusion body formation in a given cell is only observable up to a wide interval. To account for this uncertainty, we incorporate an interval-censored Weibull model for the time of inclusion body formation into our hierarchical model. Again, this ensures that the uncertainty associated with not knowing the exact time of IB formation is properly accounted for.

Posterior samples from the model were generated by Markov chain Monte Carlo using JAGS software through the rjags interface to R.

4.17 FRET ANALYSIS

Neurons expressing the ATP FRET sensor were imaged in CFP, YFP, and FRET (CFP excitation/ YFP emission) channels. Mean fluorescence intensities for each neuron were

extracted via Pipeline Pilot. Normalized FRET was calculated as described previously (*116*). CFP and Venus bleed-through values under the FRET filter set were calculated as described previously (*116*) from neurons transfected with CFP alone or Venus alone imaged under the CFP, YFP, and FRET filter sets. 20 neurons each were used to calculate CFP and Venus bleed-through values.

CHAPTER 5.

DISCUSSION

5.1 CAVEATS OF THE MITOPHAGY ASSAY

Here, we established a new flux assay that measures mitochondrial turnover in live neurons and can be applied on a single-cell basis. We found that the measured mitochondrial half-life is responsive to modulators of mitochondrial health, mitophagy, and autophagy, indicating that the mitochondrial clearance measured with this assay is mediated primarily by mitophagy. In a primary neuron model of HD, we found that neurons with mHtt IBs had slower rates of mitophagy than neurons expressing diffuse mHtt. Finally, and perhaps most notably, we used Bayesian regression analysis to show that fast mitochondrial turnover is associated with reduced neuronal longevity in cells expressing Htt, implicating mitochondrial clearance as an indicator of Htt-mediated toxicity in HD.

Since the discovery of PINK1 and Parkin, which have been implicated in Parkinson's disease (*65*), as regulators of mitophagy (*38*), interest in this pathway has grown. However, the lack of sensitive and quantitative assays of mitophagy has limited the investigation of the importance of mitophagy in neurodegenerative disease. Here, we designed and validated a live-cell mitophagic flux assay that is robust, quantitative, and adaptable to multiple model systems. In addition to enabling, for the first time, the measurement of mitochondrial clearance on an individual cell basis, the assay can also be adapted as a screening platform for the discovery of modulators of neuronal mitophagy. As mitophagy has been studied primarily in non-neuronal cells, and as it is likely that autophagy and mitophagy are regulated differently in neurons than in non-neuronal cells (*66*, *67*), the discovery of these modulators will likely lead to novel insights regarding mitochondrial quality control in neurons.

Although our assay is sensitive to modulators of the mitophagy and autophagy pathway, none of the pharmacological or genetic inhibitors we tested resulted in a complete block of autophagy or mitophagy – the changes in half-life we observed were incremental. Neurons are postmitotic cells that rely heavily on intracellular protein quality control pathways, such as autophagy, to maintain protein quality (rather than cell division) (*117*). Many of the inhibitors of the autophagy pathway that we tested were highly toxic to the neurons, indicating that large changes in autophagy may result in cell death. Thus, it is likely that the neurons that survived the autophagy manipulation were also the neurons that underwent incremental, rather than dramatic, changes in mitochondrial half-life. This relationship could explain why we were only able to observe incremental changes in mitochondrial half-life in response to autophagy and mitophagy manipulation. Implementing the assay in a cell type that is less sensitive to inhibition of protein quality control pathways, such as a cell line, would potentially allow for larger effects on mitochondrial half-life to be measured.

In addition, the experiments we performed do not rule out the possibility that other clearance pathways could be contributing to the reduction of the red mitoEOS2 signal that we observe. MitoEOS2 throughout the entire cell is photoswitched but the red signal is only measured in the cell body. Net mitochondrial transport into or out of the cell body could result in an increase or decrease in red mitoEOS2 that would appear as a change in mitophagic rate. In addition, a number of other autophagy-independent mitochondrial clearance pathways exist. Individual mitochondrial matrix proteins can be degraded via ATP-dependent proteases, such as Lon and ClpXP, which are derived from bacterial proteases and highly conserved in eukaryotes (*118*). These proteases degrade dysfunctional proteins into peptides, which are then degraded further by

intramitochondrial peptidases (*119*). Although these proteases degrade native mitochondrial proteins, it is possible that a foreign protein such as EOS2 could be tagged as misfolded or damaged and targeted for degradation, thereby resulting in a reduction of mitoEOS2 signal that could be misread as mitophagic clearance. Another mitochondrial protein degradation mechanism involves mitochondria-derived vesicles (MDVs), which bud off mitochondria and contain a specific set of cargo proteins targeted for degradation. These MDVs ultimately fused with lysosomes for degradation of their contents in a parkin and PINK1-dependent manner (*120*).

More recent work has identified multiple pathways that can clear whole mitochondria that are autophagy-independent. Mitochondrial degradation in lens and erythroid cells occurred normally in autophagy-deficient $Atg5^{-/-}$ mice (*121*). In addition, mitochondria are taken up into the yeast vacuole in the absence of Atg5 and Atg12 (*122*). Although these findings have not been demonstrated in neurons, these data demonstrate that mitochondrial degradation can occur in the absence of key proteins necessary for general autophagy. Finally, mitochondria can be extruded from the cell and degraded extracellularly in some contexts (*123*, *124*). Overall, additional work will be necessary to determine the contribution of each of these degradation pathways to the reduction in red mitoEOS2 signal we observe.

The half-life we measured using our mitophagy assay was 100 hours, on average. This is significantly shorter than previously published brain mitochondrial half lives, which range from 20 to 30 days (*125-127*). One potential explanation for this discrepancy is that many of the previously published studies use radioactive pulse chase techniques, which are sensitive to significant amino acid recycling and thus can overestimate half life (*128*). In addition, many of

these studies assayed mitochondrial half-life in whole brain, which includes glia and neurons as well as many neuronal subtypes. Our studies were performed in cortical neurons only, which may exhibit significant differences in metabolism and turnover that could result in a shorter mitochondrial half-life. Also, as discussed above, non-mitophagy clearance pathways could contribute to the reduction in mitoEOS2 signal we observed, thus artificially lowering the measured mitochondrial half-life. The peculiarities of the culture system could also contribute to the difference in measured half-life: the cells assayed are embryonic, and cell culture is a stressor compared to the *in vivo* milieu, which could lead to faster turnover (*129*). Finally, mis-targeting of mitoEOS2 such that some proportion of protein is degraded in the intermembrane space or outside of the mitochondria could also contribute to the half-life discrepancy we observe. In general, as there are many potential contributors to the half-life measurement that may disqualify it from being an absolute measure of mitochondrial half-life, the assay's usefulness is more as a relative measure of mitochondrial clearance across multiple conditions of interest.

5.2 IMPLICATIONS FOR SELECTIVE NEURODEGENERATION

Our results uncovered considerable diversity in the capacity of individual neurons to clear mitochondria, both in the presence and absence of Htt. We observed a variation in basal half-life of up to two orders of magnitude, consistent with previous work which showed up two three orders of magnitude variation in mitochondrial protein turnover rates (*129*). Significant evidence also points to neuronal subtype-specific differences in mitochondrial quality control mechanisms. Wild-type mouse cortex exhibited more mitochondria-containing autophagosomes than wild-type striatum, indicating that basal mitophagy levels may be lower in the striatum than in the cortex (*88*). In addition, striatal neurons are more sensitive to reduction of Omi/HtrA2

levels by mHtt expression (*52*). Omi/HtrA2 is a mitochondrial chaperone and protease that regulates autophagy (*51*, *130*). Thus, there is evidence that striatal neurons, which are the primary neuronal subtype that degenerate in HD, have altered mitochondrial quality control pathways (*131*). Such cell-to-cell variation in mitochondrial quality control suggests a potential mechanism for cell specificity in neurodegenerative disease. Previous work from our lab demonstrated that a cell's capacity to degrade Htt via its protein quality control mechanisms was predictive of its survival (*85*). Thus, variation in mitochondrial quality control could also contribute substantially to a given cell's susceptibility to mitochondrial and other stressors. Many proteins involved in neurodegenerative disease, including Aβ, alpha-synuclein, Htt, and TDP43, have been shown to induce mitochondrial dysfunction (*132*). The neuronal populations affected in these diseases are all initially limited to a single neuronal subtype; thus, it is likely that cell-to-cell variability in mitochondrial quality control mechanisms contributes to susceptibility to the toxic proteins that cause neurodegenerative disease.

5.3 MODELING HD

In this study, we modeled HD by overexpressing N-terminal (exon 1) mHtt in primary neurons, which recapitulates many features of human HD (*29*). N-terminal mHtt mouse models of HD also exhibit numerous phenotypes consistent with human HD, including motor dysfunction, muscle wasting, and reduced lifespan (*133*). Although these models reproduce many of the features observed in human HD, the exon 1 fragment used in this study and others represents less than 3% of the full-length Htt protein. In particular, the protein encoded by exon 1 does not contain important post-translational modification sites, including S421, that are known to regulate mHtt toxicity (*134*, *135*). In addition, caspase 6 proteolysis of the full-length protein,

which also contributes to mHtt toxicity, is not captured in an exon 1 model (*136*). Finally, recent work has implicated C-terminal portions of Htt in the regulation of autophagy and mitophagy (*55*, *56*). These portions of Htt were not encompassed in these studies, and their inclusion could substantially change the results of our experiments.

Although our primary neuron model of HD recapitulated many features of HD observed both in human patients and other model systems, we were unable to demonstrate significant mitochondrial dysfunction in our model. Other than an increase in ROS levels, we did not find any deficits in mitochondrial ATP production, mitochondrial membrane potential, mitochondrial mass, or mitochondrial morphology in the presence of mHtt. In fact, we observed small increases in mitochondrial membrane potential and mitochondrial length and size, pointing to potential mitochondrial compensation for increased bioenergetics demands in the presence of mHtt. Although a number of different mitochondrial deficits have been described in many different HD models, some have also found increases in mitochondrial function in the presence of mHtt (*137-139*). Many other studies have found no change in mitochondrial function in the presence of mHtt (*139-142*). It is unclear why some studies are able to demonstrate mitochondrial dysfunction in HD, while others are not. A contributing factor may be the ability of cells to compensate in the presence of toxic stimuli. Patients with HD remain asymptomatic until their 40s or even later, demonstrating that mHtt does not acutely damage neurons but does so over time as the compensatory mechanisms begin to lose their effectiveness. It may be that different HD model systems have different levels of compensatory mechanisms at play, thereby mitigating (or not) the degree to which the toxic effects of mHtt on mitochondria can be observed.

5.4 POTENTIAL MECHANISMS OF HUNTINGTIN-MEDIATED MODULATION OF AUTOPHAGY AND MITOPHAGY

We used Bayesian regression analysis to determine the relationship between mitochondrial clearance, Htt expression, IB formation, and neuronal longevity. As we have shown previously, mHtt expression is associated with reduced neuronal survival, while IB formation is associated with improved neuronal survival (*24*, *29*). Unexpectedly, we found that increased mitochondrial clearance is actually associated with reduced neuronal longevity in both mutant and wild-type Htt-expressing neurons. However, in neurons expressing GFP alone, mitochondrial clearance was associated with increased longevity. Our results indicate that basally, mitochondrial clearance via mitophagy is a marker for improved survival. In the context of Htt expression, however, mitochondrial clearance is a toxic pathway that promotes cell death. Htt can act as a scaffold for autophagy-related proteins. As both Htt and mHtt were overexpressed in our studies, it is possible that overexpression of these proteins resulted in higher-than-normal levels of scaffolding of autophagy-related proteins, and overactive autophagy. Indeed, overactive mitophagy has previously been shown to lead to cell death (*143*). Too much of a normal function of a polyQ protein leading to cell death has previously been demonstrated in spinal bulbar muscular atrophy (SBMA), where normal interactions of the androgen receptor with transcriptional coregulators were the cause of toxicity in an SBMA *Drosophila* model (*144*, *145*). However, as levels of both wild-type and mHtt increased, mitochondrial clearance rates went down, indicating an effort by the cell to compensate for overactive autophagy and mitophagy by downregulating these pathways (Fig. 5.1) and thereby improving survival. In addition, the effect of mHtt expression on mitophagy is stronger than the effect of wild-type Htt on mitophagy (Fig. 3.9d,e), indicating that the presence of the polyQ expansion may additionally

contribute to mitophagy downregulation. Although further studies will be necessary to determine the mechanism by which Htt regulates autophagy, we have implicated mitochondrial clearance as a critical driver in neurodegeneration in HD.

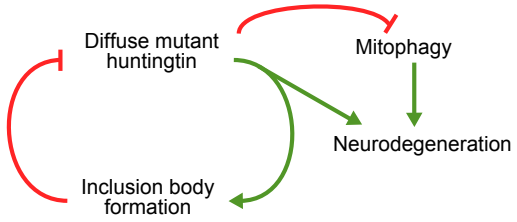


Figure 5.1 A model for the effect of mHtt on mitochondrial clearance, IB formation, and neurodegeneration. Diffuse mutant huntingtin levels predict IB formation, and IB formation reduces diffuse mutant huntingtin levels, thereby serving as a coping response. In this study, we find that, although the presence of overexpressed mHtt induces mitophagy, increasing mHtt levels are associated with reduced mitophagy. In the context of mHtt expression, mitophagy is toxic.

Prior to undertaking the Bayesian modeling approach to understand the relationships between different covariates, we observed that neurons containing IBs had slower autophagic and mitophagic turnover than neurons containing diffuse mHtt. This led us to ask whether it was the formation of an IB itself or the elevated levels of mHtt present in neurons with IBs. Using our covariate analysis, we determined that it was in fact levels of mHtt, not the IB, which determined mitophagy rates. However, we also demonstrated that cells with IBs had lower levels of autophagy-related proteins such as p62 and optineurin than cells with diffuse mHtt. Thus, it is possible that a combination of factors causes the slow autophagy and mitophagy rates in neurons with IBs.

5.5 CLINICAL IMPLICATIONS

Our findings have widespread ramifications for the development of therapeutics for HD and other neurodegenerative diseases. We have developed a novel assay that measures mitophagy dynamically in individual neurons and can be used as a screening platform for future studies looking for regulators of neuronal mitophagy for basic science or drug development purposes. In addition, our previous studies have shown that neuronal proteostasis capacity is a critical driver of neurodegeneration and can be harnessed therapeutically (*67*, *85*, *146*). Here we demonstrate that mitochondrial quality control pathways are also critical in determining neuronal longevity both basally and in the presence of Htt. Although previous attempts to use mitochondrially-targeted therapeutics, such as coenzyme Q10, in HD clinical studies have failed (*147*), no studies have been conducted specifically targeting mitochondrial quality control pathways. Recent efforts focusing on protein quality control pathways such as autophagy have focused on stimulating autophagy as a therapeutic mechanism. This study suggests that a nonspecific stimulation of autophagy or mitophagy could promote toxicity instead of preventing it. Overall, careful further studies are necessary to determine exactly how mitochondrial quality control pathways can be modulated to serve as a therapy for HD.

BIBLIOGRAPHY

1. F. O. Walker, Huntington's disease. *Lancet*. **369**, 218–228 (2007).

2. T. Foroud, J. Gray, J. Ivashina, P. M. Conneally, Differences in duration of Huntington's disease based on age at onset. *J. Neurol. Neurosurg. Psychiatr.* **66**, 52–56 (1999).

3. N. Mahant, E. A. McCusker, K. Byth, S. Graham, Huntington Study Group, Huntington's disease: clinical correlates of disability and progression. *Neurology*. **61**, 1085–1092 (2003).

4. A. Feigin *et al.*, Functional decline in Huntington's disease. *Mov. Disord.* **10**, 211–214 (1995).

5. F. Squitieri, M. Cannella, M. Simonelli, CAG mutation effect on rate of progression in Huntington's disease. *Neurol. Sci.* **23 Suppl 2**, S107–8 (2002).

6. G. A. Graveland, R. S. Williams, M. DiFiglia, Evidence for degenerative and regenerative changes in neostriatal spiny neurons in Huntington's disease. *Science*. **227**, 770–773 (1985).

7. J. P. Vonsattel *et al.*, Neuropathological classification of Huntington's disease. *J. Neuropathol. Exp. Neurol.* **44**, 559–577 (1985).

8. J. P. Vonsattel, M. DiFiglia, Huntington disease. *J. Neuropathol. Exp. Neurol.* **57**, 369–384 (1998).

9. K. Kieburtz *et al.*, Trinucleotide repeat length and progression of illness in Huntington's disease. *J Med Genet*. **31**, 872–874 (1994).

10. M. Duyao *et al.*, Trinucleotide repeat length instability and age of onset in Huntington's disease. *Nat Genet*. **4**, 387–392 (1993).

11. Y. Trottier, V. Biancalana, J. L. Mandel, Instability of CAG repeats in Huntington's disease: relation to parental transmission and age of onset. *J Med Genet*. **31**, 377–382 (1994).

12. S. E. Andrew *et al.*, The relationship between trinucleotide (CAG) repeat length and clinical features of Huntington's disease. *Nat Genet*. **4**, 398–403 (1993).

13. R. G. Snell *et al.*, Relationship between trinucleotide repeat expansion and phenotypic variation in Huntington's disease. *Nat Genet*. **4**, 393–397 (1993).

14. D. R. Langbehn *et al.*, A new model for prediction of the age of onset and penetrance for Huntington's disease based on CAG length. *Clin. Genet.* **65**, 267–277 (2004).

15. H. T. Orr, H. Y. Zoghbi, Trinucleotide repeat disorders. *Annu Rev Neurosci*. **30**, 575–621 (2007).

16. M. L. Maat-Schieman *et al.*, Distribution of inclusions in neuronal nuclei and dystrophic

neurites in Huntington disease brain. *J. Neuropathol. Exp. Neurol.* **58**, 129–137 (1999).

17. M. DiFiglia *et al.*, Aggregation of huntingtin in neuronal intranuclear inclusions and dystrophic neurites in brain. *Science*. **277**, 1990–1993 (1997).

18. K. A. Sieradzan *et al.*, Huntington's disease intranuclear inclusions contain truncated, ubiquitinated huntingtin protein. *Exp Neurol*. **156**, 92–99 (1999).

19. S. W. Davies *et al.*, Formation of neuronal intranuclear inclusions underlies the neurological dysfunction in mice transgenic for the HD mutation. *CELL*. **90**, 537–548 (1997).

20. M. W. Becher *et al.*, Intranuclear neuronal inclusions in Huntington's disease and dentatorubral and pallidoluysian atrophy: correlation between the density of inclusions and IT15 CAG triplet repeat length. *Neurobiol Dis*. **4**, 387–397 (1998).

21. F. Saudou, S. Finkbeiner, D. Devys, M. E. Greenberg, Huntingtin acts in the nucleus to induce apoptosis but death does not correlate with the formation of intranuclear inclusions. *CELL*. **95**, 55–66 (1998).

22. M. Kim *et al.*, Mutant huntingtin expression in clonal striatal cells: dissociation of inclusion formation and neuronal survival by caspase inhibition. *J Neurosci*. **19**, 964–973 (1999).

23. I. A. Klement *et al.*, Ataxin-1 Nuclear Localization and Aggregation. *CELL*. **95**, 41–53 (1998).

24. M. Arrasate, S. Mitra, E. S. Schweitzer, M. R. Segal, S. Finkbeiner, Inclusion body formation reduces levels of mutant huntingtin and the risk of neuronal death. *Nature*. **431**, 805–810 (2004).

25. S. Mitra, S. Finkbeiner, The ubiquitin-proteasome pathway in Huntington's disease. *ScientificWorldJournal*. **8**, 421–433 (2008).

26. D. L. Stenoien *et al.*, Polyglutamine-expanded androgen receptors form aggregates that sequester heat shock proteins, proteasome components and SRC-1, and are suppressed by the HDJ-2 chaperone. *Hum Mol Genet*. **8**, 731–741 (1999).

27. S. Waelter *et al.*, Accumulation of mutant huntingtin fragments in aggresome-like inclusion bodies as a result of insufficient protein degradation. *Mol Biol Cell*. **12**, 1393–1407 (2001).

28. A. Yamamoto, J. J. Lucas, R. Hen, Reversal of neuropathology and motor dysfunction in a conditional model of Huntington's disease. *CELL*. **101**, 57–66 (2000).

29. J. Miller *et al.*, Quantitative relationships between huntingtin levels, polyglutamine length, inclusion body formation, and neuronal death provide novel insight into huntington's disease molecular pathogenesis. *Journal of Neuroscience*. **30**, 10541–10550

(2010).

30. S. Finkbeiner, Huntington's Disease. *Cold Spring Harb Perspect Biol*. **3** (2011), doi:10.1101/cshperspect.a007476.

31. R. A. Nixon, The role of autophagy in neurodegenerative disease. *Nat Med*. **19**, 983–997 (2013).

32. M. Wong, Mammalian Target of Rapamycin (mTOR) Pathways in Neurological Diseases. *Biomed J*. **36**, 40 (2013).

33. Y. Wei, S. Pattingre, S. Sinha, M. Bassik, B. Levine, JNK1-mediated phosphorylation of Bcl-2 regulates starvation-induced autophagy. *Molecular Cell*. **30**, 678–688 (2008).

34. A. Williams *et al.*, Novel targets for Huntington's disease in an mTOR-independent autophagy pathway. *Nat Chem Biol*. **4**, 295–305 (2008).

35. F. M. Menzies, K. Moreau, D. C. Rubinsztein, Protein misfolding disorders and macroautophagy. *Curr Opin Cell Biol*. **23**, 190–197 (2011).

36. S. Sarkar, Regulation of autophagy by mTOR-dependent and mTOR-independent pathways: autophagy dysfunction in neurodegenerative diseases and therapeutic application …. *Biochem. Soc. Trans* (2013), doi:10.1016/j.stem.2009.11.009.

37. B. Boland *et al.*, Autophagy induction and autophagosome clearance in neurons: relationship to autophagic pathology in Alzheimer's disease. *Journal of Neuroscience*. **28**, 6926–6937 (2008).

38. D. Narendra, A. Tanaka, D.-F. Suen, R. J. Youle, Parkin is recruited selectively to impaired mitochondria and promotes their autophagy. *J Cell Biol*. **183**, 795–803 (2008).

39. P. Gómez-Suaga *et al.*, Leucine-rich repeat kinase 2 regulates autophagy through a calcium-dependent pathway involving NAADP. *Hum Mol Genet*. **21**, 511–525 (2012).

40. F. M. Laird *et al.*, Motor neuron disease occurring in a mutant dynactin mouse model is characterized by defects in vesicular trafficking. *Journal of Neuroscience*. **28**, 1997–2005 (2008).

41. N. Morimoto *et al.*, Increased autophagy in transgenic mice with a G93A mutant SOD1 gene. *Brain Res*. **1167**, 112–117 (2007).

42. D. D. O. Martin, S. Ladha, D. E. Ehrnhoefer, M. R. Hayden, Autophagy in Huntington disease and huntingtin in autophagy. *Trends Neurosci*. **38**, 26–35 (2015).

43. K. B. Kegel *et al.*, Huntingtin expression stimulates endosomal-lysosomal activity, endosome tubulation, and autophagy. *Journal of Neuroscience*. **20**, 7268–7278 (2000).

44. Petersén A *et al.*, Expanded CAG repeats in exon 1 of the Huntington's disease gene

stimulate dopamine-mediated striatal neuron autophagy and degeneration. *Hum Mol Genet*. **10**, 1243–1254 (2001).

45. M. Martinez-Vicente *et al.*, Cargo recognition failure is responsible for inefficient autophagy in Huntington's disease. *Nat Neurosci*. **13**, 567–576 (2010).

46. B. Ravikumar *et al.*, Inhibition of mTOR induces autophagy and reduces toxicity of polyglutamine expansions in fly and mouse models of Huntington disease. *Nat Genet*. **36**, 585–595 (2004).

47. Y. C. Wong, E. L. F. Holzbaur, The Regulation of Autophagosome Dynamics by Huntingtin and HAP1 Is Disrupted by Expression of Mutant Huntingtin, Leading to Defective Cargo Degradation. *Journal of Neuroscience*. **34**, 1293–1305 (2014).

48. S. Zheng *et al.*, Deletion of the huntingtin polyglutamine stretch enhances neuronal autophagy and longevity in mice. *PLoS Genet.* **6**, e1000838 (2010).

49. A. Kuhn, D. Thu, H. J. Waldvogel, R. L. M. Faull, R. Luthi-Carter, Population-specific expression analysis (PSEA) reveals molecular changes in diseased brain. *Nat Methods*. **8**, 945–947 (2011).

50. A. Hodges *et al.*, Regional and cellular gene expression changes in human Huntington's disease brain. *Hum Mol Genet*. **15**, 965–977 (2006).

51. B. Li *et al.*, Omi/HtrA2 is a positive regulator of autophagy that facilitates the degradation of mutant proteins involved in neurodegenerative diseases. *Cell Death Differ*. **17**, 1773–1784 (2010).

52. R. Inagaki *et al.*, Omi / HtrA2 is relevant to the selective vulnerability of striatal neurons in Huntington's disease. *Eur J Neurosci*. **28**, 30–40 (2008).

53. B. Baldo, R. Soylu, Å. Petersén, Maintenance of Basal Levels of Autophagy in Huntington's Disease Mouse Models Displaying Metabolic Dysfunction. *PLoS ONE*. **8**, e83050 (2013).

54. D. D. O. Martin *et al.*, Identification of a post-translationally myristoylated autophagy-inducing domain released by caspase cleavage of huntingtin. *Hum Mol Genet*. **23**, 3166–3179 (2014).

55. J. S. Steffan, Does Huntingtin play a role in selective macroautophagy? *Cell Cycle*. **9**, 3401–3413 (2010).

56. J. Ochaba *et al.*, Potential function for the Huntingtin protein as a scaffold for selective autophagy. *Proc Natl Acad Sci USA* (2014), doi:10.1073/pnas.1420103111.

57. Y.-N. Rui *et al.*, Huntingtin functions as a scaffold for selective macroautophagy. *Nat Cell Biol* (2015), doi:10.1038/ncb3101.

58. W.-X. Ding, X.-M. Yin, Mitophagy: mechanisms, pathophysiological roles, and analysis. *Biol. Chem.* **393**, 547–564 (2012).

59. G. Ashrafi, T. L. Schwarz, The pathways of mitophagy for quality control and clearance of mitochondria. *Cell Death Differ* (2012), doi:10.1038/cdd.2012.81.

60. D. F. Egan *et al.*, Phosphorylation of ULK1 (hATG1) by AMP-activated protein kinase connects energy sensing to mitophagy. *Science*. **331**, 456–461 (2011).

61. F. Strappazzon *et al.*, AMBRA1 is able to induce mitophagy via LC3 binding, regardless of PARKIN and p62/SQSTM1. *Cell Death Differ* (2014), doi:10.1038/cdd.2014.139.

62. A. Orvedahl *et al.*, Image-based genome-wide siRNA screen identifies selective autophagy factors. *Nature*. **480**, 113–117 (2011).

63. I. Novak *et al.*, Nix is a selective autophagy receptor for mitochondrial clearance. *EMBO reports*. **11**, 45–51 (2010).

64. M. Lazarou *et al.*, The ubiquitin kinase PINK1 recruits autophagy receptors to induce mitophagy. *Nature*. **524**, 309–314 (2015).

65. E. Deas, N. W. Wood, H. Plun-Favreau, Mitophagy and Parkinson's disease: the PINK1-parkin link. *Biochim Biophys Acta*. **1813**, 623–633 (2011).

66. V. S. Van Laar *et al.*, Bioenergetics of neurons inhibit the translocation response of Parkin following rapid mitochondrial depolarization. *Hum Mol Genet*. **20**, 927–940 (2011).

67. A. S. Tsvetkov *et al.*, A small-molecule scaffold induces autophagy in primary neurons and protects against toxicity in a Huntington disease model. *Proceedings of the National Academy of Sciences*. **107**, 16982–16987 (2010).

68. Q. Cai, H. M. Zakaria, A. Simone, Z.-H. Sheng, Spatial Parkin Translocation and Degradation of Damaged Mitochondria via Mitophagy in Live Cortical Neurons. *Curr Biol*. **22**, 545–552 (2012).

69. T. L. Schwarz, Mitochondrial trafficking in neurons. *Cold Spring Harb Perspect Biol*. **5** (2013), doi:10.1101/cshperspect.a011304.

70. G. Amadoro *et al.*, Morphological and bioenergetic demands underlying the mitophagy in post-mitotic neurons: the pink-parkin pathway. *Front. Ag. Neurosci.* **6**, 18 (2014).

71. M. P. Mattson, M. Gleichmann, A. Cheng, Mitochondria in neuroplasticity and neurological disorders. *Neuron*. **60**, 748–766 (2008).

72. A. V. Panov *et al.*, Early mitochondrial calcium defects in Huntington's disease are a direct effect of polyglutamines. *Nat Neurosci*. **5**, 731–736 (2002).

73. I. S. Seong *et al.*, HD CAG repeat implicates a dominant property of huntingtin in mitochondrial energy metabolism. *Hum Mol Genet*. **14**, 2871–2880 (2005).

74. W. Song *et al.*, Mutant huntingtin binds the mitochondrial fission GTPase dynamin-related protein-1 and increases its enzymatic activity. *Nat Med*. **17**, 377–382 (2011).

75. A. L. Orr *et al.*, N-terminal mutant huntingtin associates with mitochondria and impairs mitochondrial trafficking. *J Neurosci*. **28**, 2783–2792 (2008).

76. L. Cui *et al.*, Transcriptional Repression of PGC-1α by Mutant Huntingtin Leads to Mitochondrial Dysfunction and Neurodegeneration. *CELL*. **127**, 59–69 (2006).

77. I. Kim, S. Rodriguez-Enriquez, J. J. Lemasters, Selective degradation of mitochondria by mitophagy. *Arch Biochem Biophys*. **462**, 245–253 (2007).

78. G. Twig *et al.*, Fission and selective fusion govern mitochondrial segregation and elimination by autophagy. *EMBO J*. **27**, 433–446 (2008).

79. G. Twig, B. Hyde, O. S. Shirihai, Mitochondrial fusion, fission and autophagy as a quality control axis: the bioenergetic view. *Biochim Biophys Acta*. **1777**, 1092–1097 (2008).

80. S. Hwang, M. H. Disatnik, D. Mochly-Rosen, Impaired GAPDH-induced mitophagy contributes to the pathology of Huntington's disease. *EMBO Mol Med*. **7**, 1307–1326 (2015).

81. B. Khalil *et al.*, PINK1-induced mitophagy promotes neuroprotection in Huntington's disease. *Cell Death Dis*. **6**, e1617 (2015).

82. K. Palikaras, N. Tavernarakis, Mitophagy in neurodegeneration and aging. *Front Genet*. **3**, 297 (2012).

83. J. Zhu, R. K. Dagda, C. T. Chu, Monitoring mitophagy in neuronal cell cultures. *Methods Mol Biol*. **793**, 325–339 (2011).

84. D. J. Klionsky *et al.*, Guidelines for the use and interpretation of assays for monitoring autophagy. *Autophagy*. **8** (2012), pp. 445–544.

85. A. S. Tsvetkov *et al.*, Proteostasis of polyglutamine varies among neurons and predicts neurodegeneration. *Nat Chem Biol* (2013), doi:10.1038/nchembio.1308.

86. T. Hering, N. Birth, J.-W. Taanman, M. Orth, Selective striatal mtDNA depletion in end-stage Huntington's disease R6/2 mice. *Exp Neurol* (2015), doi:10.1016/j.expneurol.2015.02.004.

87. M. Damiano *et al.*, Tissue- and Cell-Specific Mitochondrial Defect in Parkin-Deficient Mice. *PLoS ONE*. **9**, e99898 (2014).

88. M. Diedrich *et al.*, Brain Region Specific Mitophagy Capacity could Contribute to Selective Neuronal Vulnerability in Parkinson's disease. *Proteome Sci*. **9**, 59 (2011).

89. S. J. Barmada *et al.*, Autophagy induction enhances TDP43 turnover and survival in neuronal ALS models. *Nat Chem Biol* (2014), doi:10.1038/nchembio.1563.

90. S. A. Mckinney, C. S. Murphy, K. L. Hazelwood, M. W. Davidson, L. L. Looger, A bright and photostable photoconvertible fluorescent protein. *Nat Methods*. **6**, 131–133 (2009).

91. N. G. Gurskaya *et al.*, Engineering of a monomeric green-to-red photoactivatable fluorescent protein induced by blue light. *Nat. Biotechnol.* **24**, 461–465 (2006).

92. H. Yu *et al.*, Gene delivery to mitochondria by targeting modified adenoassociated virus suppresses Leber's hereditary optic neuropathy in a mouse model. *Proc Natl Acad Sci USA*. **109**, E1238–47 (2012).

93. M. Arrasate, S. Finkbeiner, Automated microscope system for determining factors that predict neuronal fate. *Proc Natl Acad Sci USA*. **102**, 3840–3845 (2005).

94. N. Livnat-Levanon, M. H. Glickman, Ubiquitin-proteasome system and mitochondria - reciprocity. *Biochim Biophys Acta*. **1809**, 80–87 (2011).

95. B. Westermann, W. Neupert, Mitochondria-targeted green fluorescent proteins: convenient tools for the study of organelle biogenesis in Saccharomyces cerevisiae. *Yeast* (2000).

96. D. C. Rubinsztein, J. E. Gestwicki, L. O. Murphy, D. J. Klionsky, Potential therapeutic applications of autophagy. *Nat Rev Drug Discov*. **6**, 304–312 (2007).

97. A. Siddiqui *et al.*, Mitochondrial DNA damage is associated with reduced mitochondrial bioenergetics in Huntington's disease. *Free radical biology & medicine*. **53**, 1478–1488 (2012).

98. M. P. Murphy, How mitochondria produce reactive oxygen species. *Biochem. J.* **417**, 1–13 (2009).

99. M. J. Calkins *et al.*, The Nrf2/ARE pathway as a potential therapeutic target in neurodegenerative disease. *Antioxid Redox Signal*. **11**, 497–508 (2009).

100. H. Imamura *et al.*, Visualization of ATP levels inside single living cells with fluorescence resonance energy transfer-based genetically encoded indicators. *Proc Natl Acad Sci USA*. **106**, 15651–15656 (2009).

101. M. W. Ward, A. C. Rego, B. G. Frenguelli, D. G. Nicholls, Mitochondrial membrane potential and glutamate excitotoxicity in cultured cerebellar granule cells. *Journal of Neuroscience*. **20**, 7208–7219 (2000).

102. H. Katayama, T. Kogure, N. Mizushima, T. Yoshimori, A. Miyawaki, A Sensitive and Quantitative Technique for Detecting Autophagic Events Based on Lysosomal Delivery. *Chemistry & Biology*. **18**, 1042–1052 (2011).

103. L. Cilenti *et al.*, Inactivation of Omi/HtrA2 protease leads to the deregulation of mitochondrial Mulan E3 ubiquitin ligase and increased mitophagy. *BBA - Molecular Cell Research*, 1–29 (2014).

104. C. Schwab, S. Yu, E. G. McGeer, P. L. McGeer, Optineurin in Huntington's disease intranuclear inclusions. *Neurosci Lett*. **506**, 149–154 (2012).

105. J. Korac *et al.*, Ubiquitin-independent function of optineurin in autophagic clearance of protein aggregates. *Journal of Cell Science*. **126**, 580–592 (2013).

106. Y. C. Wong, E. L. F. Holzbaur, Optineurin is an autophagy receptor for damaged mitochondria in parkin-mediated mitophagy that is disrupted by an ALS-linked mutation. *Proc Natl Acad Sci USA* (2014), doi:10.1073/pnas.1405752111.

107. G. Skibinski, K. Nakamura, M. R. Cookson, S. Finkbeiner, Mutant LRRK2 Toxicity in Neurons Depends on LRRK2 Levels and Synuclein But Not Kinase Activity or Inclusion Bodies. *Journal of Neuroscience*. **34**, 418–433 (2014).

108. S. Mitra, A. S. Tsvetkov, S. Finkbeiner, Single neuron ubiquitin-proteasome dynamics accompanying inclusion body formation in huntington disease. *J Biol Chem*. **284**, 4398–4403 (2009).

109. K. J. Jager, P. C. van Dijk, C. Zoccali, F. W. Dekker, The analysis of survival data: the Kaplan-Meier method. *Kidney Int.* **74**, 560–565 (2008).

110. J. Miller *et al.*, Identifying polyglutamine protein species in situ that best predict neurodegeneration. *Nat Chem Biol*. **7**, 925–934 (2011).

111. P. K. Andersen, R. D. Gill, Cox's Regression Model for Counting Processes: A Large Sample Study on JSTOR. *The annals of statistics* (1982).

112. T. Lindeberg, Feature Detection with Automatic Scale Selection. *International Journal of Computer Vision*. **30**, 79–116 (1998).

113. H. Kong, H. C. Akakin, S. E. Sarma, A generalized Laplacian of Gaussian filter for blob detection and its applications. *IEEE Trans Cybern*. **43**, 1719–1733 (2013).

114. J. Schindelin *et al.*, Fiji: an open-source platform for biological-image analysis. *Nat Methods*. **9**, 676–682 (2012).

115. L.-K. Huang, M.-J. J. Wang, Image thresholding by minimizing the measures of fuzziness. *Pattern Recognition*. **28**, 41–51 (1995).

116. Z. Xia, Y. Liu, Reliable and global measurement of fluorescence resonance energy

transfer using fluorescence microscopes. *Biophys. J.* **81**, 2395–2402 (2001).

117. E. Eden *et al.*, Proteome half-life dynamics in living human cells. *Science*. **331**, 764–768 (2011).

118. M. Koppen, T. Langer, Protein degradation within mitochondria: versatile activities of AAA proteases and other peptidases. *Crit. Rev. Biochem. Mol. Biol.* **42**, 221–242 (2007).

119. T. Tatsuta, T. Langer, Quality control of mitochondria: protection against neurodegeneration and ageing. *EMBO J*. **27**, 306–314 (2008).

120. G.-L. McLelland, V. Soubannier, C. X. Chen, H. M. Mcbride, E. A. Fon, Parkin and PINK1 function in a vesicular trafficking pathway regulating mitochondrial quality control. *EMBO J* (2014), doi:10.1002/embj.201385902.

121. M. Matsui, A. Yamamoto, A. Kuma, Y. Ohsumi, N. Mizushima, Organelle degradation during the lens and erythroid differentiation is independent of autophagy. *Biochem Biophys Res Commun*. **339**, 485–489 (2006).

122. D. Mijaljica, M. Prescott, R. J. Devenish, Different fates of mitochondria: alternative ways for degradation? *Autophagy*. **3**, 4–9 (2007).

123. K. G. Lyamzaev *et al.*, Novel mechanism of elimination of malfunctioning mitochondria (mitoptosis): formation of mitoptotic bodies and extrusion of mitochondrial material from the cell. *Biochim Biophys Acta*. **1777**, 817–825 (2008).

124. C.-H. O. Davis *et al.*, Transcellular degradation of axonal mitochondria. *Proc Natl Acad Sci USA* (2014), doi:10.1073/pnas.1404651111.

125. M. S. Rajwade, S. S. Katyare, P. Fatterpaker, Regulation of mitochondrial protein turnover by thyroid hormone (s). *Biochemical …* (1975).

126. R. A. Menzies, P. H. Gold, The turnover of mitochondria in a variety of tissues of young adult and aged rats. *J Biol Chem*. **246**, 2425–2429 (1971).

127. D. S. Beattie, R. E. Basford, S. B. Koritz, The turnover of the protein components of mitochondria from rat liver, kidney, and brain. *J Biol Chem*. **242**, 4584–4586 (1967).

128. S. Miwa, C. Lawless, T. von Zglinicki, Correction of radiolabel pulse-chase data by a mathematical model: application to mitochondrial turnover studies. *Biochem. Soc. Trans*. **38**, 1322–1328 (2010).

129. X. C. Y. Chan, C. M. Black, A. J. Lin, P. Ping, E. Lau, Mitochondrial protein turnover: methods to measure turnover rates on a large scale. *J. Mol. Cell. Cardiol.* **78**, 54–61 (2015).

130. T. Clausen, C. Southan, M. Ehrmann, The HtrA family of proteases: implications for protein composition and cell fate. *Molecular Cell*. **10**, 443–455 (2002).

131. J. Margulis, S. Finkbeiner, Proteostasis in striatal cells and selective neurodegeneration in Huntington's disease. *Frontiers in Cellular Neuroscience* (2014), doi:10.3389/fncel.2014.00218/abstract.

132. E. Lezi, R. H. Swerdlow, Mitochondria in neurodegeneration. *Adv. Exp. Med. Biol.* **942**, 269–286 (2012).

133. L. Mangiarini *et al.*, Exon 1 of the HD gene with an expanded CAG repeat is sufficient to cause a progressive neurological phenotype in transgenic mice. *CELL*. **87**, 493–506 (1996).

134. H. Rangone, G. Poizat, J. Troncoso, The serum- and glucocorticoid-induced kinase SGK inhibits mutant huntingtin-induced toxicity by phosphorylating serine 421 of huntingtin - Rangone - 2004 - European Journal of Neuroscience - Wiley Online Library. *European Journal of ...* (2004).

135. R. Pardo, Inhibition of Calcineurin by FK506 Protects against Polyglutamine-Huntingtin Toxicity through an Increase of Huntingtin Phosphorylation at S421. *Journal of Neuroscience*. **26**, 1635–1645 (2006).

136. R. K. Graham *et al.*, Cleavage at the caspase-6 site is required for neuronal dysfunction and degeneration due to mutant huntingtin. *CELL*. **125**, 1179–1191 (2006).

137. J. Oláh *et al.*, Increased glucose metabolism and ATP level in brain tissue of Huntington's disease transgenic mice. *FEBS J.* **275**, 4740–4755 (2008).

138. I. L. Ferreira *et al.*, Bioenergetic dysfunction in Huntington's disease human cybrids. *Exp Neurol*. **231**, 127–134 (2011).

139. J. J. Pellman, J. Hamilton, T. Brustovetsky, N. Brustovetsky, Ca(2+) Handling in Isolated Brain Mitochondria and Cultured Neurons Derived from the YAC128 Mouse Model of Huntington's Disease. *J Neurochem* (2015), doi:10.1111/jnc.13165.

140. P. Guidetti *et al.*, Early degenerative changes in transgenic mice expressing mutant huntingtin involve dendritic abnormalities but no impairment of mitochondrial energy production. *Exp Neurol*. **169**, 340–350 (2001).

141. J. M. A. Oliveira *et al.*, Mitochondrial dysfunction in Huntington's disease: the bioenergetics of isolated and in situ mitochondria from transgenic mice. *J Neurochem*. **101**, 241–249 (2007).

142. J. Hamilton, J. J. Pellman, T. Brustovetsky, R. A. Harris, N. Brustovetsky, Oxidative metabolism in YAC128 mouse model of Huntington's disease. *Hum Mol Genet* (2015), doi:10.1093/hmg/ddv209.

143. L. Chakrabarti, J. Eng, N. Ivanov, G. A. Garden, A. R. La Spada, Autophagy activation and enhanced mitophagy characterize the Purkinje cells of pcd mice prior to neuronal death. *Mol Brain*. **2**, 24 (2009).

144. N. B. Nedelsky *et al.*, Native functions of the androgen receptor are essential to pathogenesis in a Drosophila model of spinobulbar muscular atrophy. *Neuron*. **67**, 936–952 (2010).

145. I. H. Kratter, S. Finkbeiner, PolyQ disease: too many Qs, too much function? *Neuron*. **67**, 897–899 (2010).

146. S. J. Barmada *et al.*, Amelioration of toxicity in neuronal models of amyotrophic lateral sclerosis by hUPF1. *Proc Natl Acad Sci USA* (2015), doi:10.1073/pnas.1509744112.

147. Huntington Study Group, A randomized, placebo-controlled trial of coenzyme Q10 and remacemide in Huntington's disease. *Neurology*. **57**, 397–404 (2001).

APPENDIX

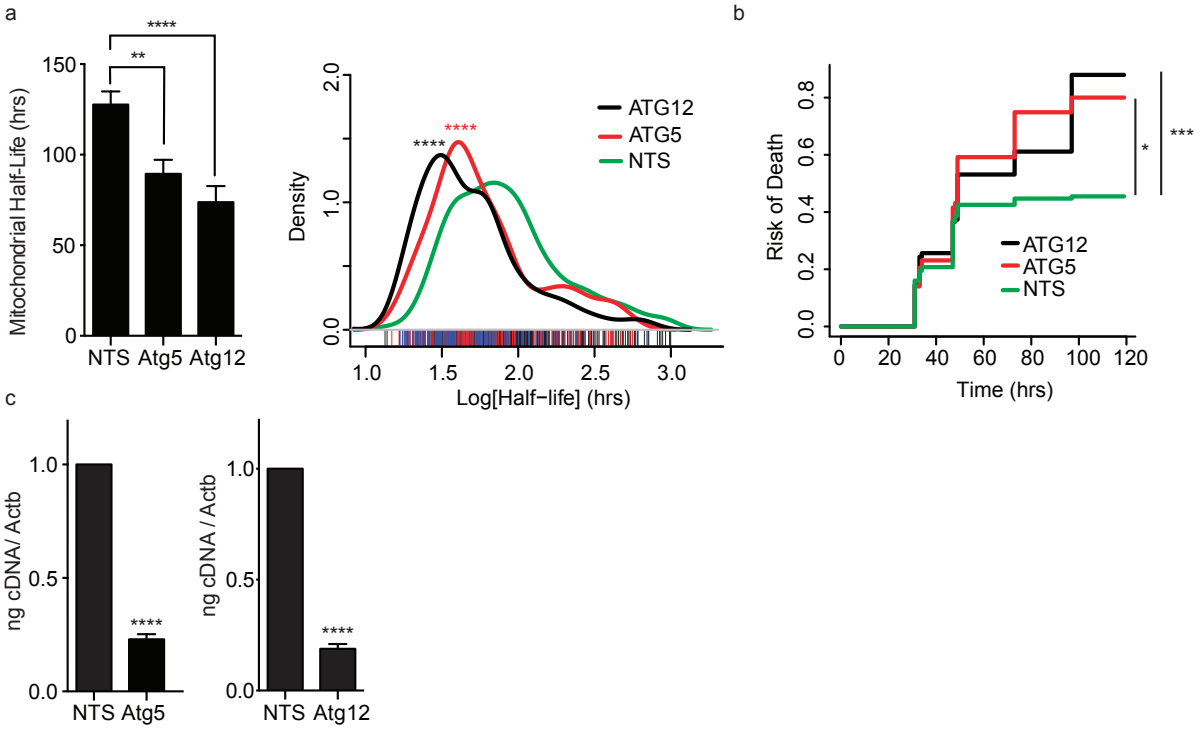


Figure A.1 Effect of Atg5/12 knockdown on neuronal mitophagy and survival. (a) Effect of Atg5/12 knockdown on mitochondrial half-life. Knockdown of both Atg5 and Atg12 signficantly reduced mean half-life (left) compared to neurons expressing non-targeting shRNA (NTS) and shifted the distribution of half-lives to the left towards shorter half-lives (right). (b) Survival curves of neurons expressing NTS, Atg5 shRNA, or Atg12 shRNA. Both Atg5 and Atg12 shRNAs reduced neuronal survival significantly. (c) Effect of Atg5/12 shRNA on Atg5/12 mRNA levels. Infection of primary neurons with Atg5/12 shRNA-expressing lentivirus results in a ~75% reduction in Atg5 mRNA levels (left) and Atg12 mRNA levels (right) as measured by qRT-PCR. Complementary DNA (cDNA) levels were normalized to levels of actin cDNA (Actb) in each sample. Means across conditions were compared using 1-way ANOVA with Dunnett's correction or Student's t-test. Distributions were compared using a Mann-Whitney-Wilcoxon test. Survival curves were compared using a log-rank test. *, p<0.05; **, p<0.01; ***, p<0.001; ****, p<0.0001

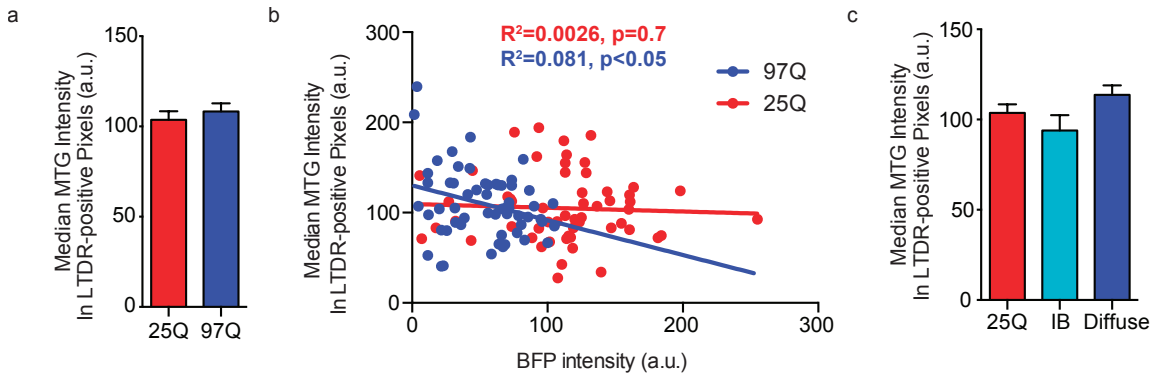


Figure A.2 Effect of mHtt expression on mitochondria-lysosome co-localization (a) Effect of Htt^{ex1}-97Q-EBFP2 expression on LysoTracker Deep Red (LTDR)-MitoTracker Green (MTG) co-localization. Neurons were thresholded based on LTDR intensity, and a mask was made of the area encompassed by lysosomes in the neuron. This mask was applied to the MTG image, and median MTG intensity in the LTDR mask was calculated. No difference was observed in MTG-LTDR co-localization between neurons expressing Htt^{ex1}-25Q-EBFP2 (25Q) or Htt^{ex1}-97Q-EBFP2 (97Q). (b) Correlation between MTG-LTDR co-localization and Htt expression represented by BFP intensity. There is no correlation between 25Q expression and MTG-LTDR co-localization (R^2=0.0026, p=0.7). Increasing 97Q expression is associated with reduced MTG-LTRD co-localization (R^2=0.081, p<0.05). (c) Effect of diffuse or IB mHtt on MTG-LTDR co-localization. There is no difference in co-localization between neurons that do and don't have mHtt IBs. Means across conditions were compared using 1-way ANOVA with Dunnett's correction or Student's t-test.

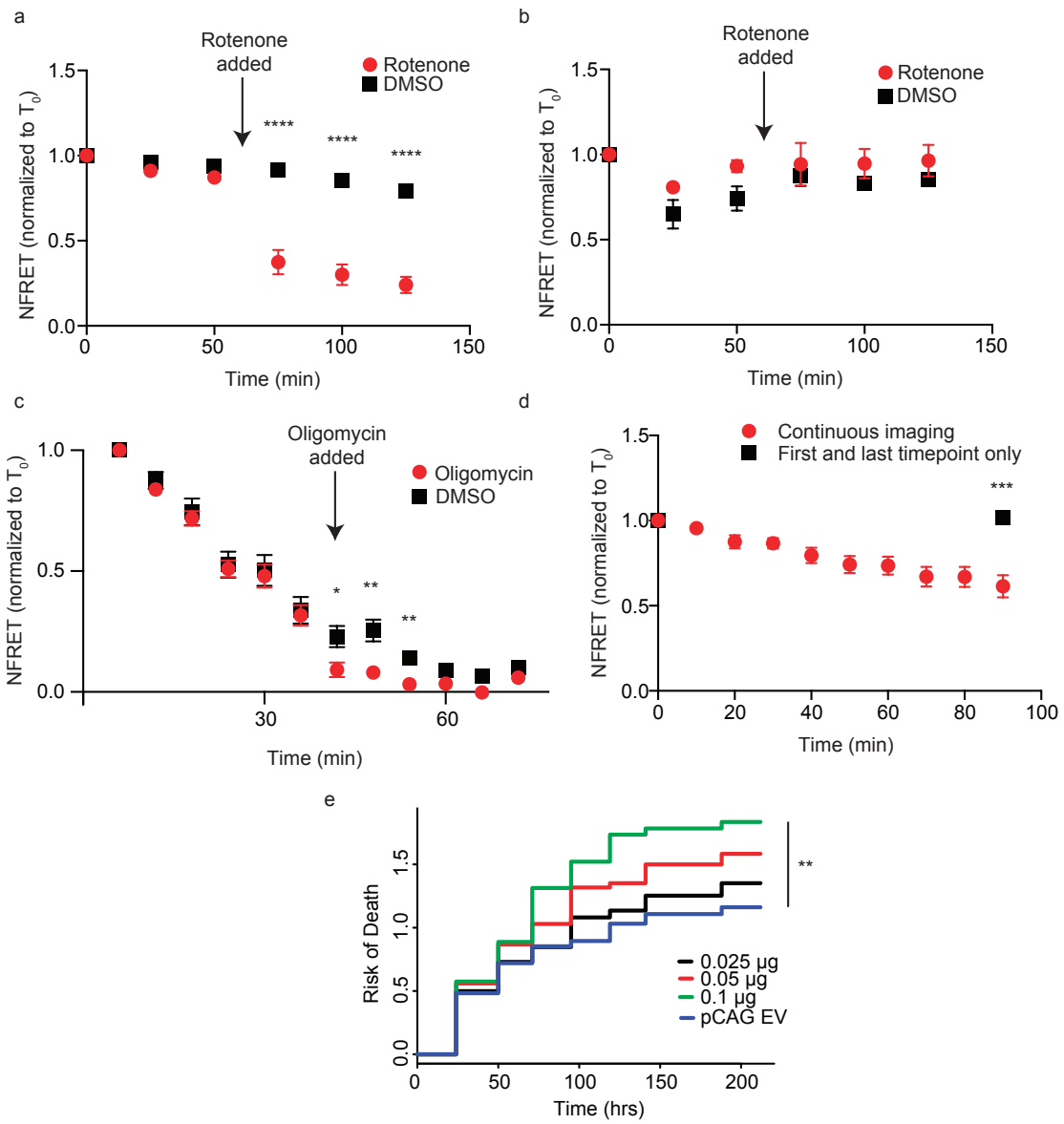


Figure A.3 Validation of FRET-based ATP assay. (a) Effect of 1 µM rotenone treatment on normalized FRET (NFRET) in neurons transfected with the ATP sensor. Rotenone significantly decreases NFRET. (b) Effect of 1 µM rotenone treatment on NFRET in neurons transfected with a CFP-Venus fusion protein that is not responsive to ATP concentration. Rotenone treatment has no effect on NFRET. (c) Effect of 1 µM oligomycin treatment on NFRET in neurons transfected with the ATP sensor. Oligomycin treatment significantly decreases NFRET. (d) Comparison of frequent (continuous) vs. infrequent (first and last) imaging on NFRET in neurons transfected with the ATP sensor. Continuous imaging results in a significant reduction in NFRET over time, potentially due to bleaching of the fluorescence signal. (e) Effect of ATP sensor expression on neuronal survival. Transfection of 0.1 µg ATP sensor significantly reduces survival compared to neurons transfected with empty vector (pCAG EV). Means across conditions were compared using Student's t-test. Survival curves were compared using a log-rank test. *, p<0.05; **, p<0.01; ***, p<0.001; ****, p<0.0001

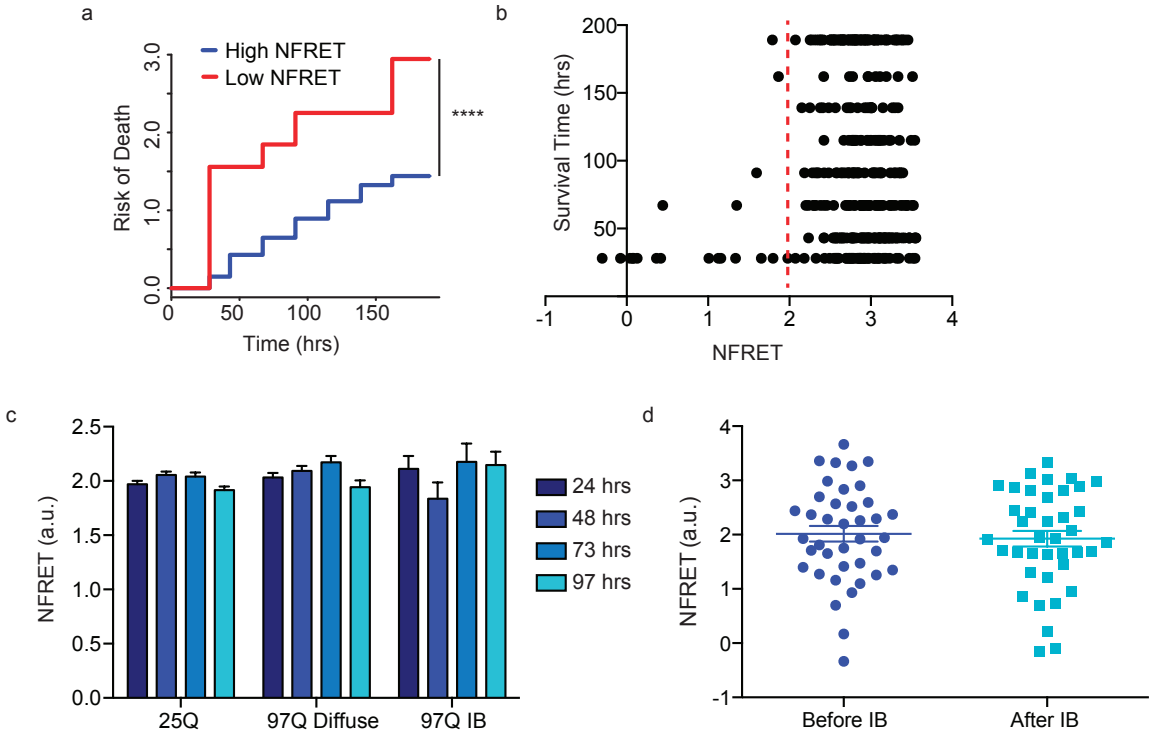


Figure A.4 Characterization of ATP signal in primary neurons. (a) Survival curves of neurons transfected with the ATP sensor that have high initial NFRET (>2) or low initial NFRET (<2). Neurons with low initial NFRET had a significantly higher risk of death than neurons with low initial NFRET. (b) Survival times of all neurons plotted vs. NFRET signal at first timepoint in each neuron. Neurons with an NFRET value <2 tend to die quickly, while neurons with higher NFRET values can live longer. (c) NFRET values of neurons transfected with Htt^{ex1}-25Q-mCherry and Htt^{ex1}-97Q-mCherry across different timepoints. 97Q-expressing neurons were segmented into cells that do or do not have IBs. There is no effect of either time or Htt expression on NFRET signal. (d) NFRET signal in a set of neurons before and after Htt^{ex1}-97Q-mCherry IB formation. There was no change in NFRET signal after IB formation. Means across conditions were compared using Student's t-test or 2-way ANOVA. Survival curves were compared using a log-rank test. *, $p<0.05$; **, $p<0.01$; ***, $p<0.001$; ****, $p<0.0001$

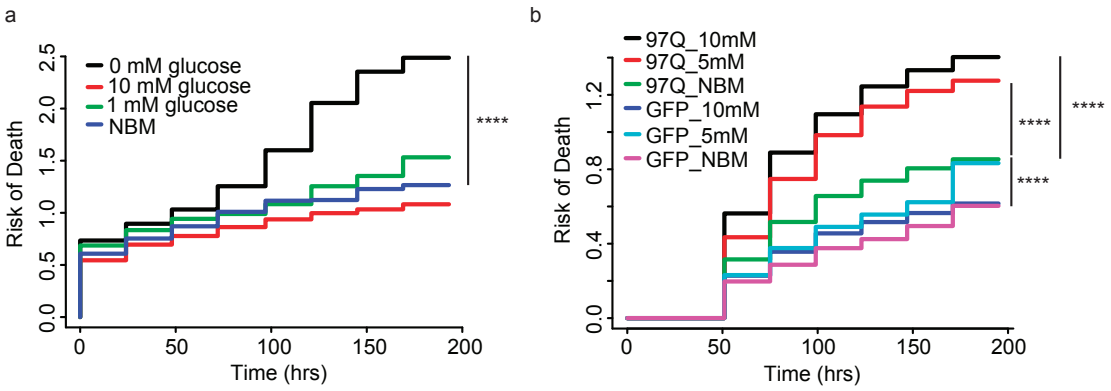


Figure A.5 Effect of low glucose media on neuronal survival and mHtt toxicity. (a) Survival curves of neurons grown in normal Neurobasal media (NBM), NBM with 10 mM glucose, NBM with 1 mM glucose, and NBM with no glucose. Neurons grown in media with no glucose survive significantly less well than neurons grown in normal NBM. (b) Survival curves of neurons expressing GFP or Htt^{ex1}-97Q-GFP, and grown in NBM, 5 mM glucose, or 10 mM glucose. GFP-expressing neurons grown in 5 mM glucose survived significantly worse than GFP-expressing neurons grown in NBM. In addition, Htt^{ex1}-97Q-GFP-expressing neurons grown in 5 mM glucose survived significantly worse than Htt^{ex1}-97Q-GFP-expressing neurons grown in NBM. All non-NBM conditions have 10 mM pyruvate supplemented in addition to the glucose concentration listed. Survival curves were compared using a log-rank test. ****, $p<0.0001$

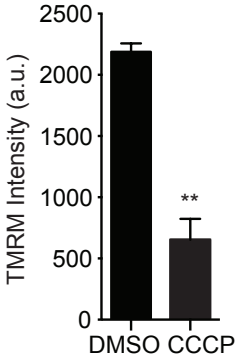
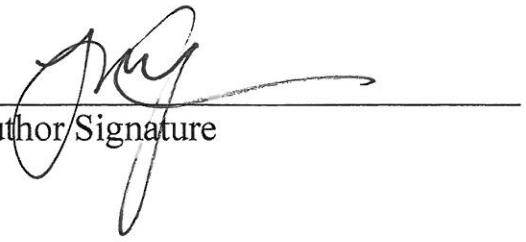


Fig A.6 Effect of CCCP treatment on TMRM intensity in neurons. TMRM-labeled neurons were treated with 1 μM CCCP for ~80 min. CCCP treatment significantly reduces TMRM fluorescence intensity in neuronal cell bodies.

Publishing Agreement

It is the policy of the University to encourage the distribution of all theses, dissertations, and manuscripts. Copies of all UCSF theses, dissertations, and manuscripts will be routed to the library via the Graduate Division. The library will make all theses, dissertations, and manuscripts accessible to the public and will preserve these to the best of their abilities, in perpetuity.

I hereby grant permission to the Graduate Division of the University of California, San Francisco to release copies of my thesis, dissertation, or manuscript to the Campus Library to provide access and preservation, in whole or in part, in perpetuity.



Author Signature

03/24/16

Date